

Coastal Aeolian Sediment Transport in an Active Bed Surface Layer

Tracer Study and Conceptual Model



Charlotte Frederike Kerstin Uphues



Committee Dr.ir. S. (Sierd) de Vries
 M.Sc. C.O. (Christa) van IJzendoorn
 Dr.ir. B.C. (Bram) van Prooijen
 Dr. G. (Graziela) Miot da Silva
 Ir. S.G. (Stuart) Pearson
 Dr.ir. E.C. (Caroline) Hallin

*Picture cover: Experimental set up for the tracer study at Noordwijk beach
(May 23, 2021 by Madelief Doeleman)*

Coastal Aeolian Sediment Transport in an Active Bed Surface Layer

Tracer Study and Conceptual Model

M.Sc. Thesis

by

Charlotte Frederike Kerstin Uphues

In partial fulfilment of the requirements for the degree of
Master of Science
in Hydraulic Engineering,
at Delft University of Technology,
to be defended publicly on October 7, 2021 at 09:00 AM.

Faculty of Civil Engineering and Geosciences,
at the Delft University of Technology

September 29, 2021

Student number: 5006201
Project duration: February 2021 - October 2021

Committee:	Dr.ir. S. de Vries	Delft University of Technology
	M.Sc. C.O. van IJzendoorn	Delft University of Technology
	Dr.ir. B.C. van Prooijen	Delft University of Technology
	Dr. G. Miot da Silva	Flinders University
	Ir. S.G. Pearson	Delft University of Technology, Deltares
	Dr.ir. E.C. Hallin	Lund University, Delft University of Technology



Preface

This thesis finalises my master studies in Hydraulic Engineering at Delft University of Technology with a specialization in Coastal Engineering. After following the course Fieldwork in Hydraulic Engineering as part of my master's program, I knew I wanted to do fieldwork as part of my MSc project. Being on the beach almost all day and doing measurements to better understand the natural occurring processes on the beach was very fascinating for me. So I was very happy when I got offered the amazing opportunity to do fieldwork in South Australia to investigate coastal dune evolution. However, travel restrictions due to the COVID 19 crisis changed the plans. Instead of South Australia I stayed in the Netherlands but I continued with the idea of doing fieldwork. I had the great opportunity to do very exciting field experiments to study coastal aeolian sediment transport in an Active Bed Surface Layer by using colored sand. This research was only possible due to the support of many people in real life and online for which I am very grateful.

First, I would like to thank all members of my graduation committee, Sierd de Vries, Christa van IJzendoorn, Bram van Prooijen, Graziela Miot da Silva, Stuart Pearson, and Caroline Hallin, for their supervision, interest and guidance during this project. Thank you, Sierd, for your support with all my ideas, for your expertise and enthusiasm during the entire project, and your guidance when I got stuck. I really appreciate the time you took for the beach visits to test out new experimental set ups and sharing your knowledge about aeolian sediment transport with me. Thank you, Christa, for all your good ideas during our weekly meetings, your time and support, and for joining the Green Light Meeting from the USA in the middle of the night. Thank you, Bram, for your constructive feedback and critical questions during the progress meetings. Your insights from a different perspective really helped me along the process of this project. Thank you, Graziela, for your positivity, for offering me the project in South Australia, and for joining all progress meetings from the other side of the world asking critical questions. I am glad that you have remained involved in the project even after South Australia got canceled. Thank you, Stuart, for sharing your enthusiasm about tracers with me, for introducing me to the digital microscope, and for your always constructive feedback. Last but not least, thank you, Caroline, for your support from Sweden, for your good ideas during our meetings, and for still taking the time to go through my report during maternity leave.

Second, I wish to express my appreciation to everyone who helped me with the preparation and execution of the field experiments. For the preparations in the waterlab I want to thank Pieter van der Gaag, Chantal Willems, and Arno Doorn, for their time and support to show me the measurement instruments, to provide me a work space, to build a wood frame for the experiments, and for always being there for me when something did not work. Ines Kodde, I owe you a big thank you for helping me sieving and coloring the sand in the waterlab and for coming to the beach with me under the most windy (and sometimes also cold and rainy) conditions to do my experiments. I also want to thank everyone from the Surf School 'Beach Break' who supported my field experiments by picking up and storing the equipment, and providing a warm and sand-free place between the experiments. Also thanks to Michiel and Madelief for assisting me with the experiments on the beach, and for taking awesome pictures of them. Thank you, Martin, for giving me Welly, the car, as a birthday present, without him the field experiments would not have been possible. A big thank you also goes to Dave for coming several times to the beach with me to perform tests and experiments, to carry heavy equipment and to always think along with me how to improve the experimental set up.

Last, I want to thank my friends and family in Germany and my 'Waterbender' friends from Delft. Thank you, Malene, for always helping me with all my questions regarding cameras and video editing, and even taking videos of you blowing sand in your apartment. Thank you, Emma, for always thinking along with me and having a listening ear. Thank you, Kira and Matze, for your encouraging words from your own experience when I needed them. Thank you, Mama, Papa, and Ami for your unconditional faith and support throughout my entire studies. I know I can always rely on you. And thank you, 'Waterbenders' for all the good times together, working on assignments, drinking beers, and talking about our different theses. You always gave me a warm and welcoming feeling and made Delft a very enjoyable place for me.

*Charlotte Uphues
Delft, September 2021*

Summary

Coastal aeolian sediment transport processes are influenced by supply limiting factors such as sediment sorting. Lighter, finer grains get eroded relatively quickly because they are easier to mobilize by the fluid drag force, while coarser particles are left behind and move slower. Such sorting processes can cause a coarsening of the bed surface and influence the formation of aeolian ripples. However, it is not fully understood what influence and importance sorting processes have on the magnitude of aeolian sediment transport. In this study, the horizontal and vertical movement of different grain sizes due to their interaction with wind is explored by performing fieldwork using tracers. The findings of the tracer study are further used to establish a conceptual model to investigate the influence of sorting processes on the magnitude of aeolian transport.

Several tracer experiments were conducted in the area between the intertidal zone and the dune toe at Noordwijk beach in the Netherlands for different wind speeds with an onshore component. Sand grains were painted in different colors according to particle size and placed in an area of 30 cm x 30 cm with a thickness of 3 cm. Three cameras tracked the sand color movement on the bed surface. Surface samples were also taken 0.5 m, 2 m, and 4 m downwind of the placement site and analyzed with a digital microscope. Additionally, wind speed and direction were measured to relate the findings to the concurrent environmental conditions.

The results show that for moderate wind conditions, the tracer sand interacted with the sediment entering the test site from upwind direction, forming aeolian ripples with coarser grains on the ripple crests and smaller grains in the ripples troughs. Once the ripples have formed, the supply of finer tracer grains in downwind direction decreased over time, while the supply of coarser grains remained constant. A strong linear relationship between ripple propagation speed and wind speed was found. For higher wind velocities, no ripples or differences in transport of different grain size fractions in downwind direction were observed. Alternating phases of erosion and deposition of upwind sand were observed after the tracer sand got partly eroded. These phases could not be related to local gradients in wind speed.

Based on these results and additions from literature, a conceptual model for an Active Bed Surface Layer (ABSL) in which sand grains interact with the wind and cause sorting was developed. The conceptual model describes the most important characteristics of the ABSL for two regimes corresponding to moderate (I), and high (II) wind speeds. These characteristics are further used to estimate their influence on the magnitude of aeolian sediment transport. For Regime I, the supply of bed sediment for saltation seems to be limited due to the formation of ripples in the ABSL and a linear relationship between sediment transport and wind speed is suggested to estimate the magnitude of aeolian sediment transport. The dynamics of the ABSL of Regime II seem to be mainly influenced by the supply of upwind sediment and spatiotemporal variations in wind speed. We propose a third power relationship between sediment transport and wind speed in combination with a process-based model that accounts for supply limitations for making aeolian sediment transport predictions.

This conceptual model of the ABSL with its two regimes describes aeolian sediment transport as a function of wind speed, bed characteristics, and upwind sediment supply. It differs from conventional aeolian sediment transport models, which only distinguish between transport and no transport and describe changes in sediment transport solely due to changes in wind speed. Thus, it can help to improve future sediment transport predictions and aeolian sediment transport models.

Thesis Structure

The main body of this thesis (Part I: Paper) is provided in paper format with the aim to publish it in the Special Issue in Earth Surface Processes and Landforms “Coastal dunes: links between aeolian processes and landform dynamics”. The appendix of this work (Part II: Additional information) is not intended to be published and provides additional information about preliminary tests and the coloring procedure of the tracer sediment. Furthermore, a user’s manual for the TU Delft wind measurement equipment is provided and an algorithm used for the post-processing of images is presented. Within Part I references to sections of Part II are provided. These references intend to guide the reader of this thesis but will not be part of the paper in the journal.

Contents

Preface	ii
Summary	iv
Thesis Structure	vi
List of Symbols	xi
I Paper	1
Abstract	2
1 Introduction	3
2 Field site and methodology	7
2.1 Field site	7
2.2 Field experiments	8
2.3 Data analysis	10
2.3.1 Automated counting of colored sediment in surface samples	10
2.3.2 Development of the bed using top view images	10
2.3.3 Changes in bed elevation using side view images	11
3 Results	12
3.1 Horizontal grain movement	12
3.1.1 Transport of different grain size fractions	12
3.1.2 Ripple migration	15
3.2 Vertical grain movement	16
4 Conceptual model for an Active Bed Surface Layer	19
4.1 Definition of an Active Bed Surface Layer (ABSL)	19
4.2 Sediment transport processes in the ABSL	20
4.2.1 Regime I	21
4.2.2 Regime II	23
5 Discussion	26
6 Conclusions	29
Bibliography	30
II Additional information	34
A Preliminary tests	35
A.1 Initial research objective	35
A.2 Test 01	35
A.2.1 Conclusions Test 01	36
A.3 Test 02	36
A.3.1 Conclusions test 02	38
A.4 Test 03	38
A.4.1 Conclusions test 03	40
A.5 New research objective	40

B	Tracer signature	41
B.1	Literature review	41
B.2	Procedure to create a tracer signature for this project	41
B.2.1	Finding the right paint	41
B.2.2	Coloring the sand	41
B.2.3	Coloring the sand per fraction	45
C	User's manual wind measurement device	47
C.1	Step 1: Checking equipment	47
C.2	Step 2: Set up wind measurement device	48
C.3	Step 3: Connecting data logger with laptop to start and read device	49
C.4	Step 4: Preliminary tests and calibration	49
C.5	Step 5: Using the wind measurement device in the field	50
C.6	Step 6: Reading out the data logger	50
C.7	Step 7: Cleaning and storing of equipment	50
D	Image analysis by using a pixel color recognition algorithm	51
D.1	Microscope images	51
D.2	GoPro images	59

List of Symbols

Symbol	Unit	Description
A	-	Empirical constant for the fluid threshold
C	-	Charnock constant
C_b	-	Grading constant
D	mm	Reference grain diameter
d	μm , mm	Grain diameter
d_{50}	μm , mm	Mean grain diameter
g	m/s^2	Gravitational acceleration
h_r	mm	Ripple height
κ	-	Von Kármán constant
p	-	Porosity
q_I	kg/m/s	Sediment transport for Regime I
q_{II}	kg/m/s	Sediment transport for Regime II
q_c	kg/m/s	Sediment transport in the form of creep
q_{cap}	kg/m/s	Sediment transport capacity by wind
q_r	kg/m/s	Sediment transport in the form of ripples
q_s	kg/m/s	Sediment transport in the form of saltation
ρ	kg/m^3	Air density
ρ_s	kg/m^3	Sediment density
τ	N/m^2	Wind shear stress
u_*	m/s	Wind shear velocity at the bed
u_{*t}	m/s	Threshold wind shear velocity
u_*/u_{*t}	-	Dimensionless wind shear velocity
u_r	mm/s	Ripple speed
u_w	m/s	Wind speed measured at a certain elevation
X	-	Up-scaling factor
z	m	Elevation above ground at which the wind speed was measured
z'_0	m	Roughness length (corresponding to the elevation at which wind speed goes to zero)



Paper

Abstract

Coastal aeolian sediment transport is influenced by supply-limiting factors such as sediment sorting by grain size. Sorting processes can cause a coarsening of the bed surface and influence the formation of aeolian ripples. However, it is not fully understood what influence sorting processes have on the magnitude of this transport. In this study, we explore sorting processes of different grain sizes when interacting with wind and their influence on the magnitude of aeolian transport by performing a tracer study and developing a conceptual model. Sand grains were painted in different colors according to particle size and placed on Noordwijk beach, Netherlands. Several experiments were conducted with varying wind speeds. Surface sampling and cameras tracked the sand color movement on the bed surface, and wind speed and direction were measured. The tracer experiments show that for moderate wind conditions, ripples developed. Once the ripples have formed, the supply of finer tracer grains in downwind direction decreased over time, while the supply of coarser grains remained constant. A strong linear relationship between ripple speed and wind speed was found. For higher wind velocities, no ripples or differences in transport of grain size fractions were observed. Alternating phases of erosion and deposition of upwind sand were observed which could not be related to local variations in wind speed. Based on these results and literature, a conceptual model for an Active Bed Surface Layer (ABSL) with two regimes corresponding to moderate (I), and high (II) wind speeds was developed. The concept enables to estimate the magnitude of aeolian sediment transport as a function of wind speed, bed characteristics, and upwind sediment supply. For Regime I, we propose a linear relationship between sediment transport and wind speed and for Regime II a third power relationship in combination with a process-based model accounting for supply limitations.

KEYWORDS: *Aeolian transport - Supply limited - Sediment sorting - Armoring - Aeolian ripples - Tracers - Beach - Field measurements - Conceptual model*

Introduction

Coastal aeolian sediment transport processes play an important role for dune evolution and therefore for coastal protection (Hesp et al., 2000). Understanding aeolian sediment transport processes is crucial for making long-term predictions of dune evolution and for determining how effectively they protect the low-lying hinterland against flooding. Many researchers have tried to predict aeolian sediment transport. However, many existing aeolian sediment transport models over-predict the actual transport rates in coastal environments (Barchyn et al., 2014; Kroon and Hoekstra, 1990; Sarre, 1989; Sherman and Li, 2012; Sherman et al., 1998). This over-prediction can be assigned to specific conditions at coastal situations that cause sediment supply to be limited (de Vries et al., 2014b). The interplay between aeolian forcing, sediment transport and sediment supply is not yet fully understood and therefore leads to uncertainties in aeolian sediment transport predictions.

Aeolian sediment transport processes occur wherever there are (1) atmospheric winds of sufficient strength and (2) a bed with granular material available for erosion (Bagnold, 1954). The flowing air of the atmospheric winds exerts a shear stress on the bed surface as a result of a net downward flow of momentum. The shear stress, τ , is the force the wind exerts on the bed surface (Sherman and Hotta, 1990):

$$\tau = \rho u_*^2 \quad (1.1)$$

where ρ is the air density (1.22 kg/m^3) and u_* is the shear velocity at the bed. For turbulent flow, the momentum transfer from the flowing air to the bed depends on the aerodynamic roughness of the bed surface, and is proportional to the change in velocity with elevation. Assuming a unidirectional, fully turbulent, uniform, and steady wind field, the shear velocity at the bed can be approximated using a logarithmic profile (Sherman and Hotta, 1990):

$$u_* = \kappa u_w / \ln\left(\frac{z}{z'_0}\right) \quad (1.2)$$

where κ is the von Kármán constant (0.4), u_w is the wind speed, at elevation z above ground, and z'_0 is the roughness length (corresponding to the elevation at which wind speed goes to zero).

When the shear stress at the bed becomes larger than the gravity and inter-particle forces of the bed particles, the bed particles are set into motion and sediment transport is initiated. Bagnold (1954) qualitatively described this sediment transport. He classified, depending on the size of the particles in motion, three different aeolian transport modes: creep, saltation and suspension (Figure 1.1). Sufficiently heavy, usually sand-sized particles ($63 \mu\text{m}$ to 2 mm) are transported along the surface in the form of creep or saltation. Creep is the movement of grains in continuous or near-continuous contact with the sand bed (Walker, 1981) and saltation is the wind driven lift-off, hopping, and splashing of particles, following long, parabolic trajectories (Bagnold, 1954). In contrast, sufficiently light particles are transported in suspension in which they are kept aloft for relatively long distances due to the turbulence of the air (Pächtz et al., 2014).

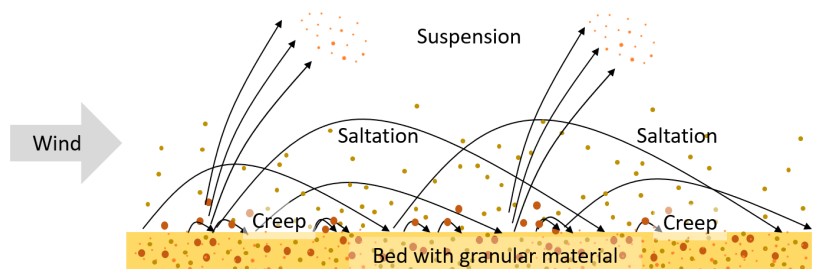


Figure 1.1: Schematic of aeolian sediment transport modes according to Bagnold (1954): Creep, saltation, and suspension. Grains of different size (brown = coarsest grains, beige = medium grains, and orange = finest grains) interact with the wind (represented as grey arrow).

Besides a qualitative description of sediment transport, Bagnold (1937) also described sediment transport in a quantitative way. He was one of the first to express the transport of bed particles in motion as the result of a direct momentum transfer from the wind. Based on wind tunnel and desert field experiments, he found a third power relationship between sediment transport and wind speed:

$$q_{cap} = C_b \sqrt{\frac{d}{D}} \frac{\rho}{g} u_*^3 \quad (1.3)$$

where C_b is a constant of 1.8 for naturally graded sand, d is grain diameter relative to a reference grain diameter D (0.24 mm (Bagnold, 1937)), and g is the gravitational acceleration. q_{cap} is the sediment transport capacity by wind which is given when the supply of sediment for erosion is unlimited.

Bagnold's approach assumes an unlimited supply of sand, however, this is often not the case on beaches. Aeolian sediment transport on beaches is often stated to be supply-limited (Houser, 2009; Nickling and Davidson-Arnott, 1990). Supply limited conditions arise when the sediment transport capacity, q_{cap} , cannot be reached due to the lack of sediment supply. Sediment supply can be limited due to bed properties (e.g., surface moisture (Davidson-Arnott et al., 2005; Schmutz and Namikas, 2018), sorting processes by grain size (Hoonhout and Vries, 2016)), profile properties (e.g., slope (Hardisty and Whitehouse, 1988; de Vries et al., 2012)), wind (e.g., fetch length (Bauer and Davidson-Arnott, 2003)), and/or the presence of physical obstructions (e.g., vegetation (Buckley, 1987), lag deposits (van der Wal, 1998; de Vries et al., 2014a), beach houses, people walking). The consequence of Bagnold-type equations not accounting for such supply-limiting factors is that they typically overestimate the transported volumes in beach environments (Sherman et al., 1998; Barchyn et al., 2014).

Many other researches followed up on Bagnold's pioneering work and formulated their own (3rd power) relationships between sediment transport and wind speed which they compared to measured sediment transport rates (e.g., Kawamura (1951); Zingg (1953); Owen (1964); Hsu (1971); Lettau and Lettau (1978); Sørensen (2004)). They all used calibration parameters in their equations which they modified to match the measured sediment transport rates. Most authors consider these calibration parameters to account for supply limiting conditions (Nickling and Davidson-Arnott, 1990; Houser, 2009). The results of the equations are partly successful (see Sherman and Li (2012); Sherman et al. (2013)). However, generic methods to derive calibration parameters are unavailable, which limits the predictive ability of any of the present transport models (Sherman and Li, 2012).

The range of factors governing coastal aeolian sediment transport is large. Continuous progress in the field of numerical area modelling enables a more comprehensive description and calculation of aeolian sediment transport by accounting for more of these factors. Hoonhout and Vries (2016) for instance developed a process-based area model supporting supply-limiting factors such as soil moisture contents, sediment sorting and armoring, bed slope effects, air humidity, and roughness elements. Durán and Moore (2013) developed an ecomorphodynamic area model to explore the influence of vegetation on the maximum size of coastal dunes. Even though a diversity of numerical area models exists, every model only focuses on a small number of the large range of factors governing coastal aeolian sediment transport. A comprehensive description of coastal aeolian sediment transport is not available.

Another problem of many existing numerical area models is that they only account for one grain size. This is a simplification, as beaches usually contain grains of widely varying sizes (well-graded beaches), which can lead to the neglect of important processes due to the saltation of differently sized grains. An exception is the model of Hoonhout and Vries (2016) which allows for the computation of aeolian sediment transport of different grain size fractions. The exchange of momentum between the sediment fractions is represented by the bed interaction parameter. This bed interaction parameter was introduced for modelling purposes and lacks validation of the underlying processes through measurements. Thus, none of the existing numerical area models is based on the occurring processes due to the saltation of differently sized grains. However, the saltation of differently sized grains can have important implications for the sediment supply from the bed.

Saltation of differently sized grains can cause sediment sorting, which can result in a coarsening of the bed surface. This is especially known and researched for rivers and often referred to as armoring (e.g., Blom (2003); Parker (2008)). In many well-graded rivers, a coarse armor layer forms on top of a subsurface layer. Lighter, finer grains get eroded relatively quickly because they are easier to mobilize by the fluid drag force, while coarser particles are left behind and move slower. Over time, the less mobile coarse particles armor the bed, precluding future erosion (Parker, 2008). Armoring can occur not only in well-graded rivers but also on well-graded beaches,

with wind instead of flowing water as fluid drag force (Hoonhout and Vries, 2016). Armor layers decrease the total transport because the surface particles available for transport tend to be coarser and more difficult to move, and are therefore a physical limit on the aeolian transport capacity. However, it is not fully understood to what degree armoring decreases the magnitude of aeolian sediment transport for different environmental conditions on the beach.

Saltation of differently sized grains can also cause the formation of aeolian ripples (Wang et al., 2019). Wind-formed ripples are distinctive bedform features of many sandy aeolian environments, and their development and migration are basic responses to sand transport via saltation (Sherman et al., 2019). Coarse and fine grains show different transport trajectories, resulting in usually coarser grains accumulating at the ripple crests and finer grains in the ripple troughs (Anderson and Bunas, 1993; Wang et al., 2019). Ripples transport sediment in the form of creep. Even though studies exist that relate creep transport associated with ripple migration to total transport rates (Sherman et al., 2019), it is not fully understood what influence and importance aeolian ripple formation and propagation has on the magnitude of aeolian sediment transport.

What all of the above mentioned supply-limiting factors have in common is that they influence the processes taking place at the interface where the wind shear stress acts on the sediment bed. This interface between the moving air and sediment bed and its near surrounding area is also the area where sediment is transported in the forms of creep and saltation (Figure 1.1). At beaches with mainly sand-sized particles, most sediment is transported in the forms of creep and saltation rather than suspension. Thus, the interface defines not only the influence area of the supply-limiting factors but also the area where most aeolian sediment transport takes place and where the interplay between wind forcing, the sediment bed and sediment transport take places. Understanding the processes at this interface is essential for making accurate aeolian sediment transport predictions. However, the physics and dynamics at this interface between wind forcing (moving air) and the sediment bed are poorly described when the quantification of aeolian sediment transport is of interest, which compromises modelling capabilities.

Several attempts to describe aeolian sediment transport involve field measurements in the interface between moving air and the sediment bed. For instance Davidson-Arnott et al. (2005), de Vries et al. (2014b), and Hoonhout and de Vries (2017) have used point measurements of wind speed and point measurements of proxies of sediment fluxes to derive/validate relationships between sediment fluxes and wind speed given the local conditions. Many existing methods to measure aeolian sediment transport in the field such as sediment traps or optical and acoustic backscatter are point measurement methods (White, 1998; Black et al., 2017). Such point measurements do not allow for a detailed analysis on the interplay between the wind, the bed, sediment transport of differently sized grains, and supply limitations.

In addition to point measurements, particle tracking, or as it is also known 'particle-' or 'sediment tracing' can provide essential insights into sediment transport processes. Particle tracing is a field method where grains are labelled or tagged and then allowed to disperse naturally with ambient currents (Black et al., 2007). The dispersal of the tracer can then be estimated based on the recovered particles. Furthermore, particle tracing seems to offer a practical solution for observing the interplay between the wind, the bed, sediment transport of differently sized grains, and supply limitations. This interplay could for instance be observed by focusing on the small-scale interaction between the tracer and non-tracer particles.

Many tracer studies have been carried out in different coastal environments (Black et al., 2007). For subaerial coastal environments, most tracer experiments took place in the temporally subaerial intertidal area (e.g., Oliveira et al. (2017); Silva et al. (2007); Kato et al. (2014); Robin et al. (2009); Vila-Concejo et al. (2004); Williams et al. (2003); Wright et al. (2015)), all with the aim of studying the distribution of the tracer by hydrodynamic-driven forces rather than by wind-driven forces. Most studies using tracers to investigate aeolian transport processes were carried out to gain insight into the interplay of large scale atmospheric, soil and land surface processes of the Earth system (Wang et al., 2017) rather than small scale transport processes of sand particles on beaches. To the best of our knowledge, aeolian sediment tracer studies in coastal environments have been carried out in dune areas to compare observed tracer sediment transport rates with theoretical models (Berg, 1983) and experimentally estimated sand trap transport rates (Cabrera and Alonso, 2010). However, no previous studies have applied tracer on beaches to investigate the small scale processes of the interplay between the wind, the bed, sediment transport of differently sized grains, and supply limitations.

In this paper we elaborate on a new concept to describe aeolian sediment transport not only as a function of

wind speed, but also of bed characteristics and supply limitations. We focus on the area where most of the sediment transport takes place: in the interface area between the bed and the moving air. First, fieldwork using tracers at a well-graded sandy beach in Noordwijk, Netherlands, in the area between the intertidal zone and the dune toe is performed to study the most important processes near and at the bed for varying wind speeds with an onshore component. The tracer experiments aim to answer the question: "How are differently sized grains transported horizontally and vertically in the interface area between the bed and the moving air by coastal aeolian sediment transport processes?". Subsequently, based on the results of the tracer study and additions from literature, a conceptual model is developed that aims to answer another question: "What influence do the processes in the interface area between the bed and the moving air have on the magnitude of aeolian sediment transport?".

Field site and methodology

A tracer study was employed to observe how differently sized grains are transported horizontally and vertically in the interface area between the bed and the moving air by coastal aeolian sediment transport processes. A fieldsite in the Netherlands with sand-sized grains being mainly exposed to winds with an onshore component was chosen. Sand grains were painted in four different colors according to particle size to observe the spatiotemporal dispersal of the differently sized tracer grains. Two types of experiments were conducted, mixed experiments and separated experiments. **Mixed** experiments (**M01 - M04**) with **Mixed** tracer sand (1/4 of each fraction) were performed to represent the naturally occurring conditions of the native sand, which contains a range of grain sizes. **Separated** experiments (**S01-S03**) with only two, **Separated** fractions, the coarsest one and a finer one, not mixed, implemented as two stripes parallel to the wind direction, were performed to test whether the tracers behave as expected in aeolian beach environments (finer grains should move more than coarser grains).

2.1 Field site

The field site for this study was the beach of Noordwijk aan Zee, located on the central Dutch coast (Figure 2.1 a) and b)). Measurements took place during the windy days from 21.05.2021 - 23.05.2021 at different locations in the area between the intertidal zone and the dune toe (Figure 2.1 b)).

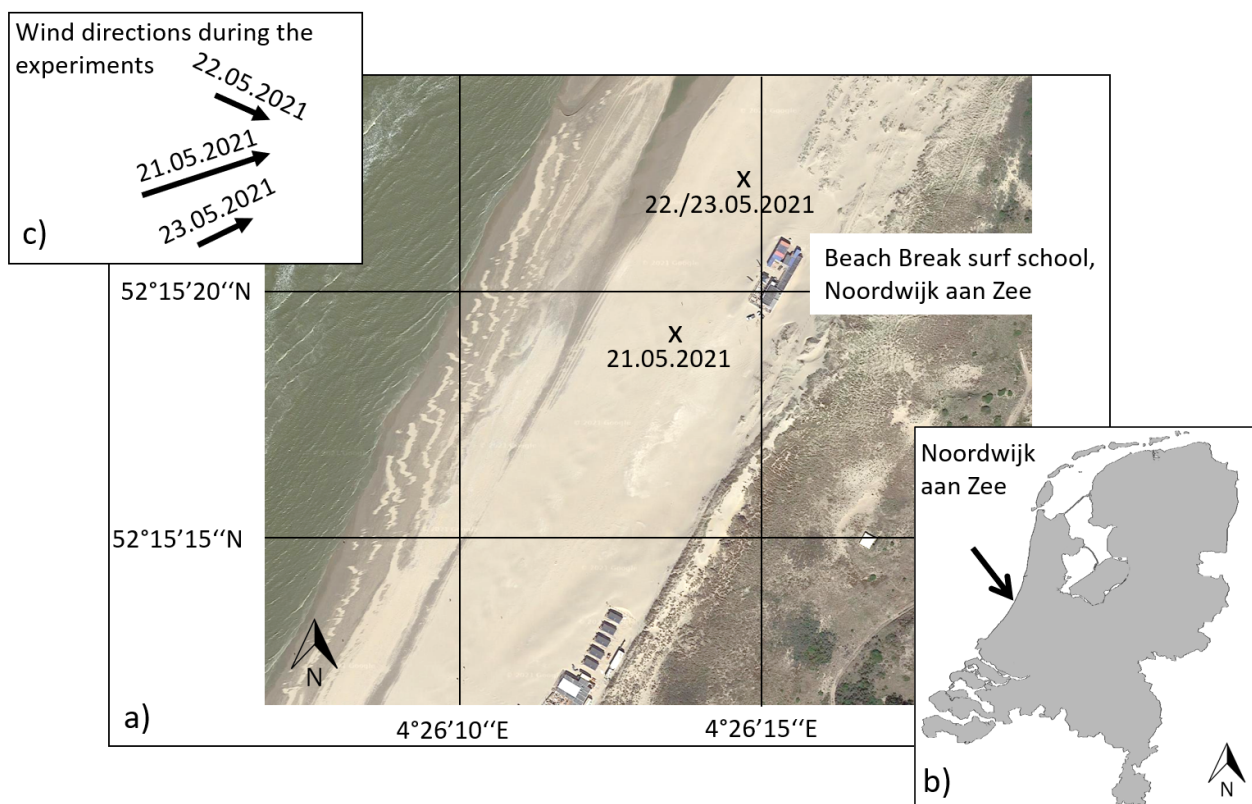


Figure 2.1: Location, orientation and appearance of the test site in Noordwijk aan Zee. a) Detailed top view of the location with indication of the areas where the experiments were performed on the 21.05.2021 and 22./23.05.2021. b) Location of the test site along the Dutch coastline. c) Identification of the mean wind directions during the three days of experiments. The length of the arrows represents qualitatively the intensity of the wind speeds.

The area consists predominantly of fine quartz sand with a mean grain size (d_{50}) of $240 \mu\text{m}$. This was estimated in a laboratory using sieving methods with native sediments collected from the top 3 cm (see black lines in Figure 2.2). The depth of 3 cm was chosen based on preliminary tests (Appendix A) which showed that the top 3 cm are most important for grain movement. The surface sand was dry on 21.05.2021 and 23.05.2021 and wet on 22.05.2021 due to heavy rainfall before the experiment and light rainfall during the experiment.

The coast of Noordwijk is wave-dominated with waves approaching the coast mainly from SW and NNW (Quartel et al., 2007). Mean wave heights and periods along the Dutch coast are 1.2 m and 5 s, respectively, and alongshore differences in wave climate are small (Wijnberg and Terwindt, 1995). The wind climate is dominated by winds from the SW with higher average wind and gust speeds during the winter months than during the summer months. The coastline is oriented SW to NE, 30° with respect to North (where the shore normal direction is 300° with respect to North). The dominant SW winds are thus oblique onshore. The tide at Noordwijk is semi-diurnal with a 1 m and a 1.8 m range at neap and spring tide, respectively (Walstra et al., 2012). The beach width is between 100 - 200 m depending on the tide.

2.2 Field experiments

Mixed (M01 - M04) and **Separated (S01-S03)** experiments with similar set ups were performed. To observe the movement of differently sized grains, native sand was sieved and colored in four different colors for four different grain size fractions ($< 0.18 \text{ mm}$: purple, $0.18 - 0.25 \text{ mm}$: green, $0.25 - 0.3 \text{ mm}$: blue, $0.3 - 0.6 \text{ mm}$: red; see Figure 2.2). The sieves were chosen according to the particle size distribution (PSD) of the native sand, so that each fraction represents approximately one quarter of the total weight. The PSD of the tracer sand mixture used for experiments M01 - M04 shows a slightly larger amount of fine grains compared to the native sand (Figure 2.2). The sieving and coloring procedure is described in more detail in Appendix B.

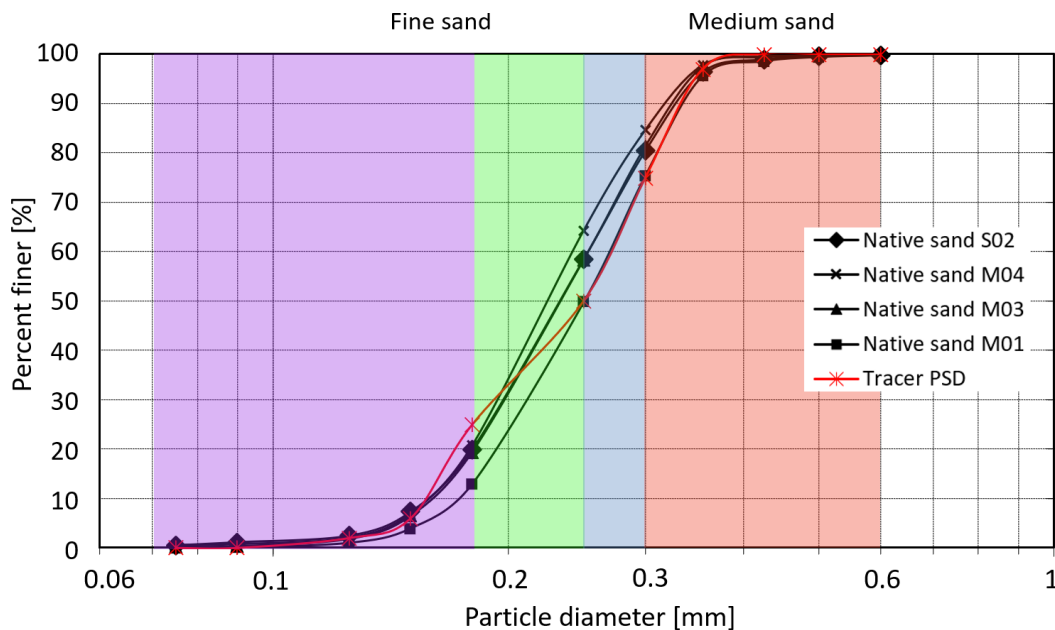


Figure 2.2: Particle size distribution (PSD) of native sand samples from the locations of the experiments M01, M03, M04, and S02 (black lines) and PSD of the tracer sand mixture which was used for experiments M01 - M04 (red line) with indication of the four colors for the four different fractions.

In the beginning of all seven experiments, a 3 cm thick layer of colored tracer sand was placed in an area of 30 cm x 30 cm, after a layer of native sand with similar thickness was removed. The dimensions of the placement area were large enough to have a representative amount of tracer grains and small enough to easily perform and repeat experiments. To protect the tracer from getting blown away during placement, the test site was protected with a removable wind screen. During experiment M01 (at 17:33), additional to the initially placed mixed tracer sand, two handfuls of mixed tracer sand (ca. 700 g in total) were poured in the wind just upwind

from the placement site to study the transport of tracer grains after the initially placed tracer sand was covered with upwind sand.

Surface samples from the top 1 mm at different distances downwind of the placement site, see Table 2.1, were taken to track the horizontal movement of the sand particles. Additional to the samples, two GoPro Hero 7 cameras (A and B) looking from above took pictures of the moving sand. Camera A observed the sediment colors present on the bed of the placement site itself, while camera B observed the sediment colors on the bed just downwind from the placement site (Figure 2.3 a)). The chosen settings for both cameras were a picture resolution of 12 megapixels (4000 × 3000 pixels), a linear field of view (FOV), and a frame rate of 1 frame per second (fps). Both cameras were mounted to a wooden frame at a height of about 20 cm above ground, taking photos of an area of about 40 cm × 30 cm each, which means that one pixel is in the order of 0.1 mm (about half the size of the mean grain diameter). In five out of the seven experiments, a third GoPro Hero 5 camera (C) with the same settings as for the other two cameras tracked the bed evolution and vertical changes in color from the side through a plexiglass screen dug in sand. This set up was developed and optimized based on preliminary tests (Appendix A).

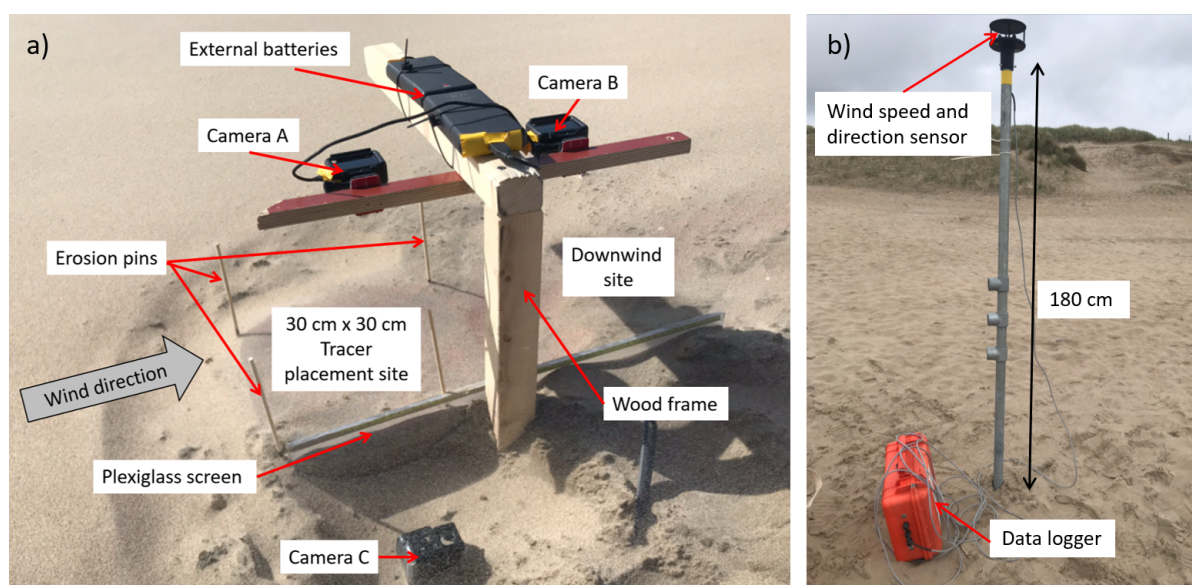


Figure 2.3: Field set up during the experiments. a) Cameras A and B mounted to a wood frame and connected to external batteries track the tracer movement from the top view. Camera C tracks the tracer movement through a plexiglass screen from the side view. b) A wind speed and direction sensor is mounted to a metal pole at a height of 180 cm above the bed and is connected to a data logger protected in an orange case.

During all experiments wind speed and direction were measured with a Gill 2D WindSonic ultrasonic wind speed and direction sensor (P/N:1405-PK-040) at a height of 180 cm above the bed. A HOBO Energy data logger (P/N: H22-001) logged the sensor at 0.5 Hz. Instructions for using the wind measurement device can be found in Appendix C. Measured local wind conditions can be found in Table 2.1 and Figure 2.1 c).

Table 2.1: Overview of experiments executed from 21.05.2021-23.05.2021. M stands for the experiments where a sand **M**ix out of all four fractions was used, while S stands for the experiments where only two **S**eparated fractions (red and green) placed as two stripes parallel to the wind direction were used. Wind speed and direction are averaged over the experiment duration, the wind speed in brackets is the maximum wind speed measured during every experiment.

Experiment	Date	Start time	End time	Top view	Side view	Samples	Average wind speed [m/s]	Average wind direction [°]
S01	21.05.2021	15:46	16:16	✓	✓	none	15.1 (21.4)	256
M01	21.05.2021	17:07	17:45	✓	✓	12 at 0.5 m	15.6 (24.4)	252
S02	21.05.2021	18:03	18:27	✓	✓	7 at 0.5 m	15.1 (21.8)	253
M02	22.05.2021	15:56	17:10	✓	✓	none	7.0 (11.2)	294
M03	23.05.2021	13:41	14:43	✓	✓	11 at 0.5 m 10 at 2 m 7 at 4 m	8.7 (12.2)	243
M04	23.05.2021	15:22	16:27	✓	x	9 at 0.5 m 3 at 2 m	7.2 (10.4)	246
S03	23.05.2021	16:37	17:12	✓	x	none	5.9 (7.9)	252

All seven experiments were performed in sufficient distance away from each other, so that the colored sand that was left after one experiment did not appear in the consecutive experiment. Table 2.1 gives an overview of all seven experiments.

2.3 Data analysis

2.3.1 Automated counting of colored sediment in surface samples

A novel method inspired by the work of Pearson et al. (2021) was developed to analyse the surface samples. All 59 collected surface samples were scanned under a Keyence VHX-5000 digital microscope (Keyence Corporation, 2014). The microscope took stitched images from every sample, which were then analysed by a pixel color recognition algorithm counting the amount of red, green, blue, and purple pixels. For every color a range for hue, saturation and value/lightness (HSV/L) was defined. The amount of colored pixels of a certain color in one image was then normalized by dividing it by the total amount of colored pixels in one image. The code of the pixel color recognition algorithm can be found in Appendix D. This novel method for analysing the samples was chosen to overcome the tedious and time-consuming part of most historical tracer studies that visually counted the number of tracer grains in a sample which is also subjected to human error (Black et al., 2007).

To test the accuracy of the pixel color recognition algorithm, three microscope images of samples with only non-colored grains were used. For all three images the algorithm counted about 0.1 % colored pixels relative to all pixels in the image. Therefore, only images where the amount of counted, colored pixels was more than 10 times larger (larger than 1 %) were taken into account for the analysis. Otherwise the influence of the erroneously counted pixels of non-colored grains (e.g., some non-colored brownish grains have some pixels that fall in the red HSV range) becomes too large and distorts the results.

2.3.2 Development of the bed using top view images

The top view images were used to determine the change of sediment color on the bed surface and to analyse ripple characteristics.

To qualitatively describe the evolution of sediment color on the bed surface, the images were edited to a timelapse video using the free software DaVinci Resolve. For a more quantitative analysis, the images were post processed using a pixel color recognition algorithm counting the amount of different colored pixels in a picture, similar to the one used for analysing the stitched images from the samples (Appendix D).

Ripple migration rates u_r were estimated by comparing the location of ripple crests in two photos that were taken 4 minutes apart from each other. The 4 minute averages of ripple speed were related to 4 minute averages in wind speed. The averaging period of 4 minutes was based on the lower limit that too short periods would result in small absolute measurement errors of the travelled ripple distances, which would grow into larger relative errors, and on the upper limit that too long periods would mask the effects of the dynamic response of the ripples to changes in wind conditions. Before each experiment, a photo was taken of a ruler placed on the ground, which was used to determine the scale in the pictures. The same ripple crest was identified and registered in subsequent photos to provide a distance traveled and this was converted to a migration rate using the time elapsed between images. The scaled images were also used to obtain estimates of ripple wavelength.

2.3.3 *Changes in bed elevation using side view images*

To track the changes in bed elevation over time, the side view images were used. For images one minute apart from each other, the line at the upper edge of the bed was traced. Then, the lines were compared to each other and intervals of erosion and sedimentation were identified. To take the influence of the plexiglass screen on the measurements into account, the side view images were compared to the accompanying top view images where the bed change was indicated by erosion pins. Only when the bed elevation close to the plexiglass was similar to the bed on the other side of the test site where no plexiglass screen was placed, the measurements were taken into account.

3.1 Horizontal grain movement

3.1.1 *Transport of different grain size fractions*

Figure 3.1 shows an example of the microscope images and the pixels captured by the pixel color recognition algorithm in this image. The algorithm captures most pixels of the colored grains, however, some very dark or light pixels of the colored grains are not captured (Figure 3.1). Additionally, some pixels of non-colored grains fall in the defined HSV range of a certain color and are counted erroneously as pixels of the colored grains (Figure 3.1).

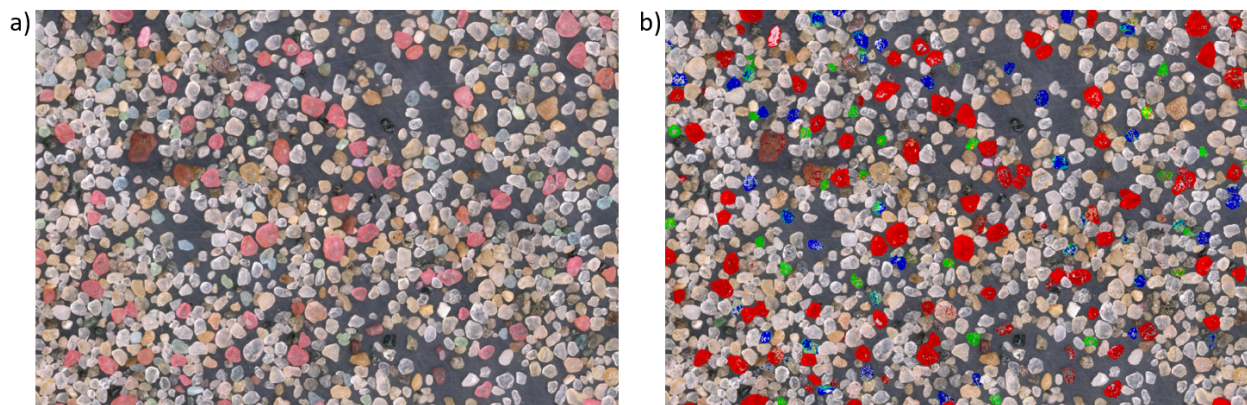


Figure 3.1: a) Extract from a microscope image of a sample downwind of the placement site. b) The same microscope image as in a) but the pixels captured by the pixel color recognition algorithm are highlighted due to an increased saturation.

Mixed sediment

For moderate wind conditions during M03 and M04, a clear signal in transport for different grain size fractions represented by differently colored pixels over time is found (Figure 3.2). After the mixed tracer sand was implemented and before ripples were formed, grains of all four fractions were exposed to the wind in a similar way at a flat surface. Shortly after placement, grains of all four fractions were found back in sediment samples at locations 0.5 m, 2 m, and 4 m away from the placement site (Figure 3.2). Over time and as ripples developed, the amount of the smaller fractions at these locations decreased (Figure 3.2 a) and c)), while the amount of coarser grains stayed almost constant (relative increase of red pixels in Figure 3.2 a) and c)), while the absolute number of colored pixels decreased, see Figure 3.2 b) and d)). This was the case for all three locations (0.5 m, 2 m and 4m away from the tracer placement site) except for the 2 m location during M04, where a slight decrease in the relative amount of red pixels over time was found. For M04, no samples were taken at 4 m because from visual inspections of the field site, no colored sediment was found there. For M03, in 24 out of 28 samples enough colored grains (represented by the relative amount of colored pixels) were found in the samples to be considered in the analysis (Figure 3.2 b) and d)). For M04, all 12 samples contained enough colored grains to be considered in the analysis (Figure 3.2 b) and d)).

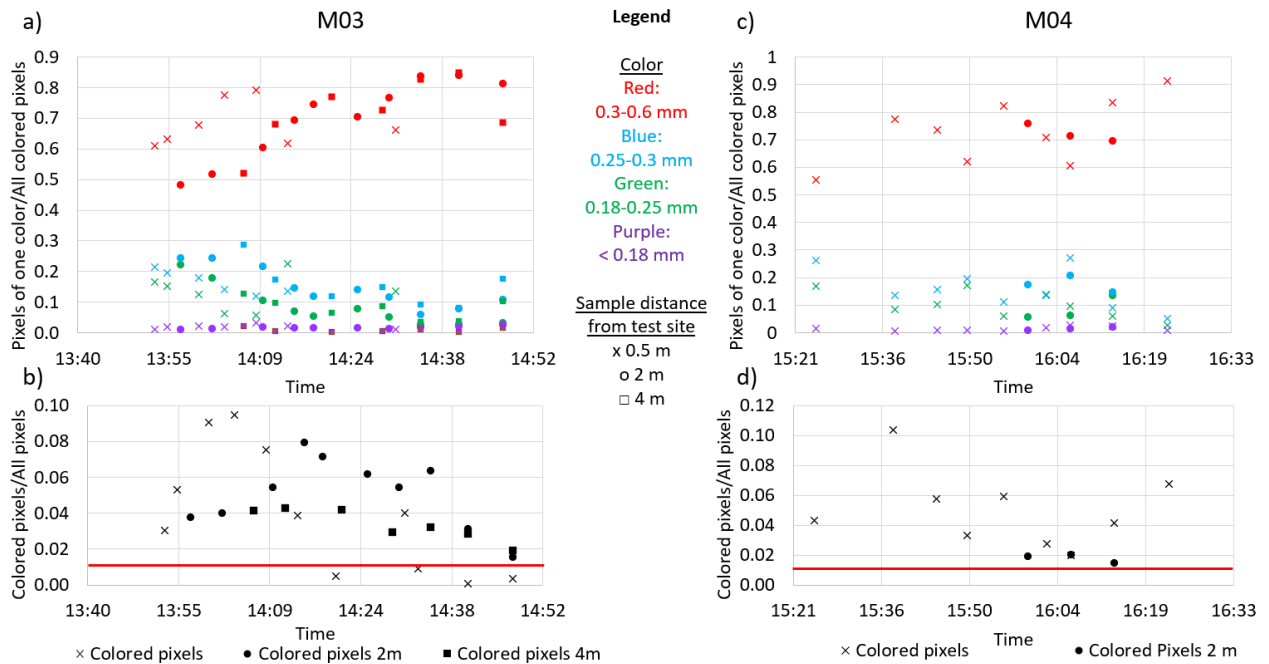


Figure 3.2: a) Normalized amount of red, green, blue and purple pixels and b) total amount of all colored pixels relative to all pixels over time found in the stitched images from surface samples during experiment M03. c) and d) show the same but during M04. For samples under the red 1 %-line in b) and d), the total amount of colored pixels w.r.t the total amount of all pixels was too small to be considered in the analysis.

For high wind conditions during M01, one part of the initially placed tracer sand was transported in downwind direction relatively quickly. The other part stayed at the placement site but got covered with upwind sand that stopped the remaining tracer sand from erosion. Hence, only the first sample had enough tracer sand to be considered in the analysis (Figure 3.3 b)). At 17:33 additional tracer sand was poured in the wind just upwind from the placement site which increased the amount of colored pixels (Figure 3.3 b)). Within three minutes (17:34 - 17:36) there are significant fluctuations in pixel counts per color (Figure 3.3 a)). At 17:37, most of the poured tracer sand was transported away, so that there was not enough colored sand in the sample to be considered in the analysis (Figure 3.3 b)).

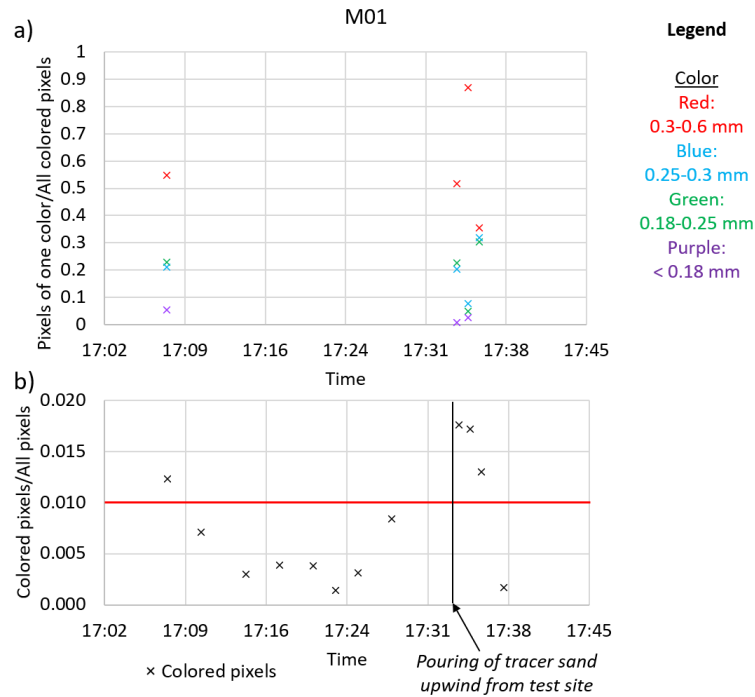


Figure 3.3: a) Normalized amount of red, green, blue and purple pixels and b) total amount of all colored pixels relative to all pixels over time found in the stitched images from the surface samples 0.5 m downwind from placement area during experiment M01. In 8 out of 12 samples (under the red 1 %-line), the total amount of colored pixels w.r.t the total amount of all pixels was too small to be considered in the analysis.

For experiment M02, no samples were taken because no sediment transport was observed. Even though the maximum measured wind speed was 11.2 m/s, the heavy rain event before and the light rain event during the experiment stopped all colored grains from moving.

Separated sediment

For moderate wind conditions during S03, the amount and distance of the smaller, green grains travelled in downwind direction is larger than for the coarser, red grains (Figure 3.4 a) and b)). This is represented by a relative increase of green pixels and an almost constant amount of red pixels over time in the top view camera images. This is in agreement with theory: smaller, lighter grains are easier to mobilize by the wind than coarser grains. This indicates that the tracer method works as expected in aeolian beach environments for moderate wind conditions.

For high wind conditions during S02, the same happened as during M01: the initially placed tracer sand got partly eroded and partly covered by upwind sediment that stopped the remaining tracer sand from erosion. Thus, in only two out of the seven samples enough colored grains were found to include in the analysis (Figure 3.4 d)). This makes it hard to make reliable statements about the individual horizontal movement of the grain size fractions (Figure 3.4 a)).

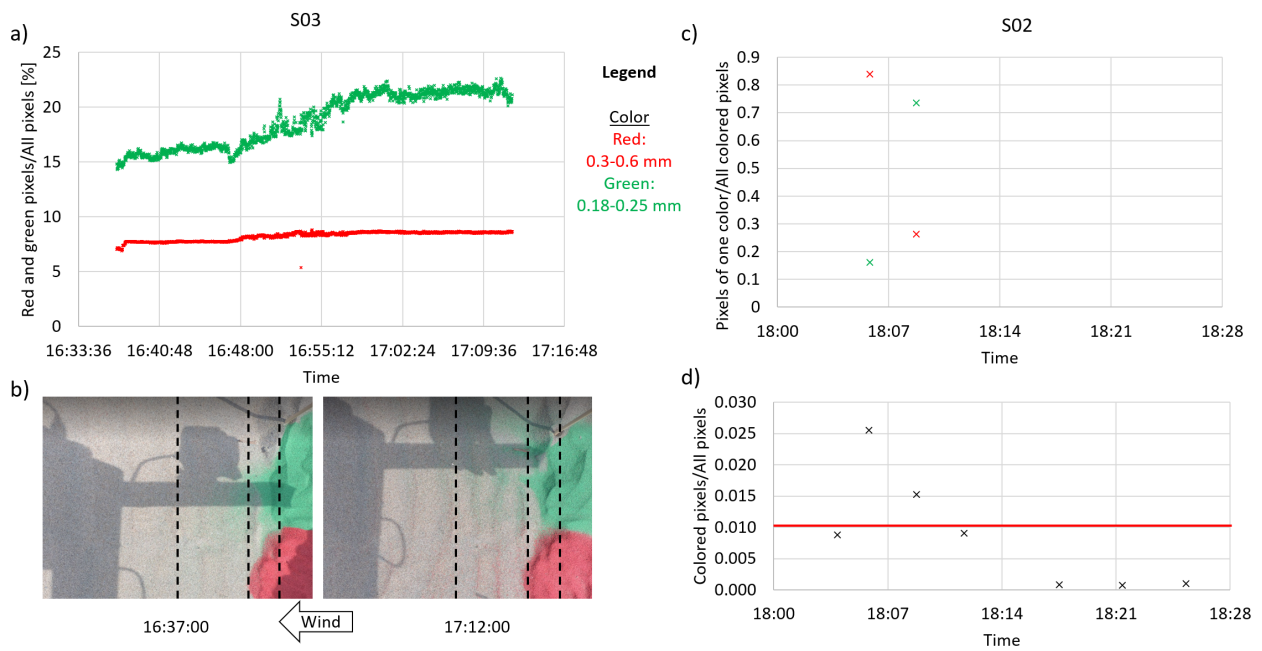


Figure 3.4: a) Amount of red and green pixels relative to all pixels over time found in Camera B images during S03. b) First and last Camera B image during S03 with black dashed lines indicating reference locations. The smaller, green grains travelled further than the larger, red ones and a larger amount of green grains was mobilized. c) Normalized amount of red and green pixels and d) total amount of all colored pixels relative to all pixels over time found in the stitched images from surface samples 0.5 m downwind from the placement area during S02. In 5 out of 7 samples (under the red 1 %-line), the total amount of colored pixels w.r.t the total amount of all pixels was too small to be considered in the analysis.

3.1.2 Ripple migration

For moderate wind conditions during M03 and M04 the formation and movement of ripples was observed (Figure 3.5). Ripple wavelengths varied between 4 cm to 10 cm with an average length of 7 cm. For high wind conditions during S01, S01, and M01 and for wet sand conditions during M02 no ripples were observed.

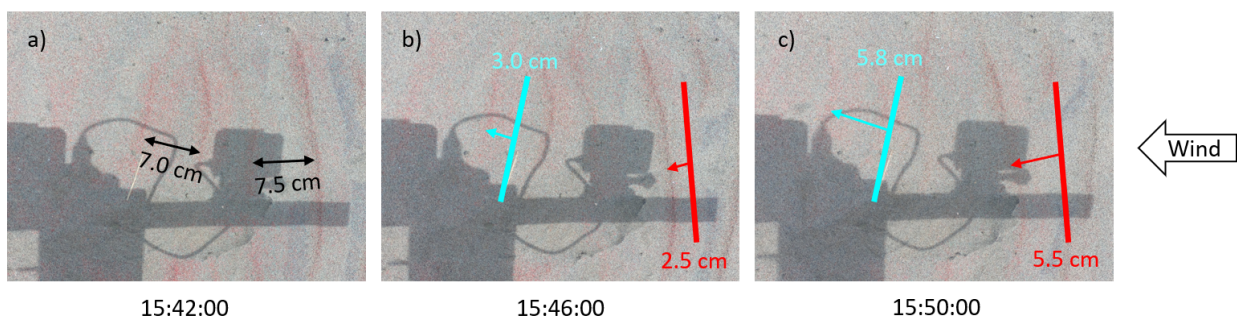


Figure 3.5: Example of ripple wavelengths and movement during M04 observed from top view Camera A images. a) Ripple wavelengths (black arrows) 20 minutes after the placement of the tracer sand. b) Movement of two individual ripple crests (red and turquoise arrows) within 4 minutes. The vertical red and turquoise lines indicate the position of the ripple crests at 15:42:00. c) Movement of two individual ripple crests (red and turquoise arrows) within 8 minutes. The vertical red and turquoise lines indicate the position of the ripple crests at 15:42:00.

Figure 3.6 shows the ripple migration rates u_r determined based on the top view images from experiments M03 and M04 and coincident wind speeds u_w at a height of 1.80 m. The 46 observations of u_r and u_w are four-minute

averages. From linear regression analysis, a relationship where $u_r = 0.085u_w - 0.54$ with $n = 46$ and $R^2 = 0.87$ is found. The four measurement points that deviate most from the mean and lie outside the 10%-quantile all occur at wind speeds above 8.2 m/s and show ripple speeds on the side above the mean.

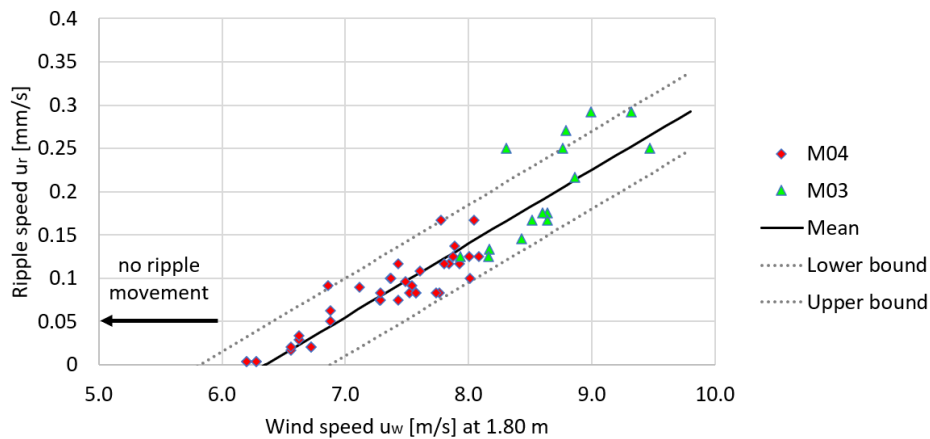


Figure 3.6: Ripple migration rate as a function of wind velocity at a height of 1.80 m ($n = 46$, $R^2 = 0.87$). The solid line indicates the mean through all measurement points, the dashed lines indicate the 10%-quantile. For 10% of the measurements, the ripple speed u_r deviates more than 0.045 mm/s from the mean value.

3.2 Vertical grain movement

To observe the vertical movement of differently sized grains, the camera images from the top and side view at different points in time were used. For moderate wind conditions, a thin layer of colored sand got eroded due to the interaction and formation of ripples with upwind sand. The coarser, red grains accumulated on the ripple crests, while the mix of finer, blue, green and purple grains accumulated in the ripple troughs (Figure 3.7). Over time, the placement site got slowly covered by ripples propagating into the site from upwind direction, stopping the remaining colored sand from movement. Patches of tracer sand were visible underneath the incoming ripples of upwind sand during the entire time of both experiments (Figure 3.7), indicating that vertical bed elevation changes were in the range of the ripple heights, which were in the order of a few millimeters.

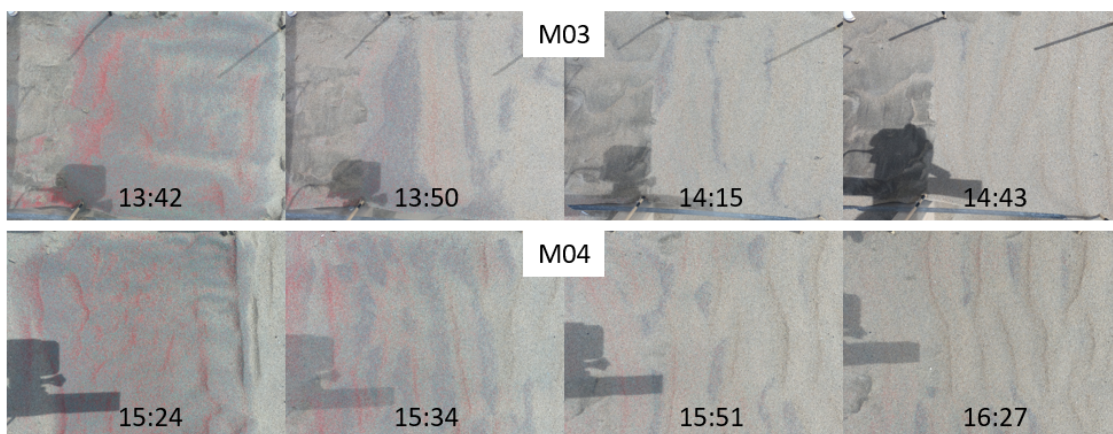


Figure 3.7: Vertical sorting of grain size fractions observed from top view Camera A images during M03 and M04: coarser, red grains accumulated on the ripple crests, while a mix of finer, blue, green and purple grains (which mix appears in the picture as dark grey areas) accumulated in the ripples troughs. Patches of tracer sand underneath incoming upwind sand ripples are visible during the entire duration of both experiment, indicating a constant bed level. Wind was blowing from right to left.

For high wind conditions, a small amount of colored sand got eroded in the beginning of the experiments S01,

M01, and S02. Then, sand from the upwind direction accreted on top of the placement site, stopping the remaining colored sand from further movement, while the sediment that was in transport was mostly provided by upwind sediment supply. The upwind sand cover on top of the tracer sand moved up and down due to phases of erosion and accretion (Figure 3.9), but the colored sand layer underneath did not get exposed again once it was fully covered by upwind sand. From the digitized side view images during S01, a total movement of the upwind sand cover of 2 cm was observed. For the experiments M01 and S02, a similar vertical movement magnitude was found from erosion pins in the top view images. This is much larger compared to the vertical bed elevation changes during moderate wind conditions which were in the range of millimeters.

In a next step, the phases of erosion and deposition from experiment S01 were related to wind speed and direction. The wind speed during S01 fluctuated around an average of 15.1 m/s with a maximum of 21.4 m/s and a minimum of 10 m/s, while the wind direction fluctuated around an average of 256 ° with a maximum of 269 ° and a minimum of 240 °. From theory, one would expect deposition (erosion) for phases of decreasing (increasing) wind speed and/or for changes in wind direction. However, only between 16:05 - 16:10 deposition was observed during a period of decreasing wind speed (Figure 3.8). Between 15:53 - 16:00 the opposite was true, erosion was observed during a period of decreasing wind speed (Figure 3.8). Thus, no clear relationship between erosion/deposition and/or wind direction/speed was found during S01.

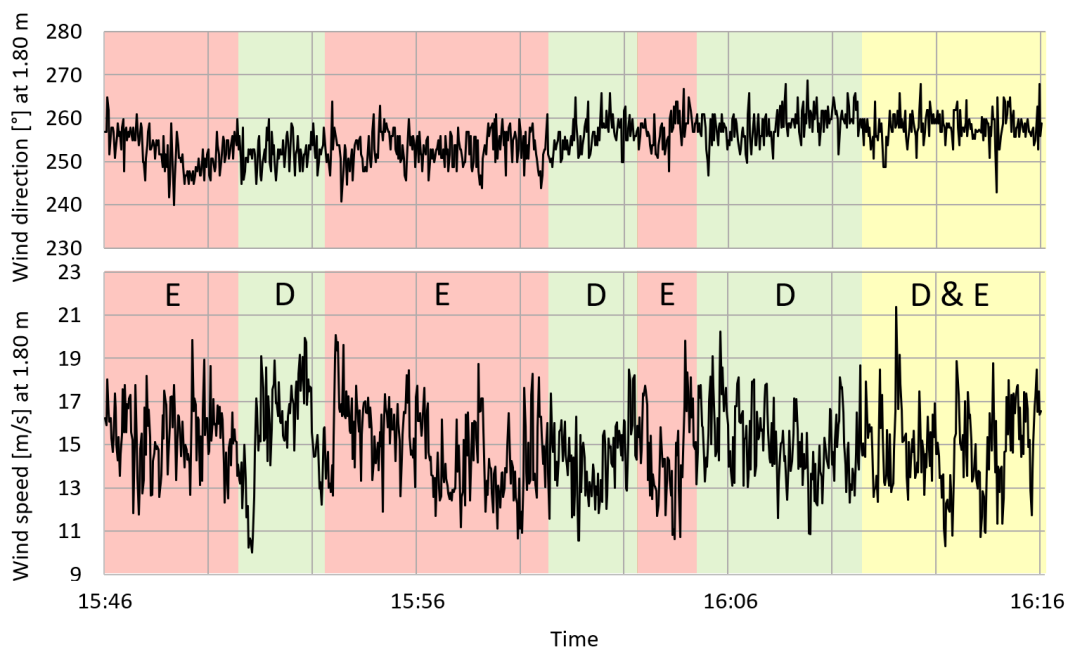


Figure 3.8: Wind direction and speed measured during S01 at a frequency of 0.5 Hz. During the red intervals (E) sediment was eroded from the placement site, while during the green intervals (D) sediment deposited. During the last, yellow interval (D & E), part of the sediment deposited on the upwind half and eroded on the right downwind half of the placement site.

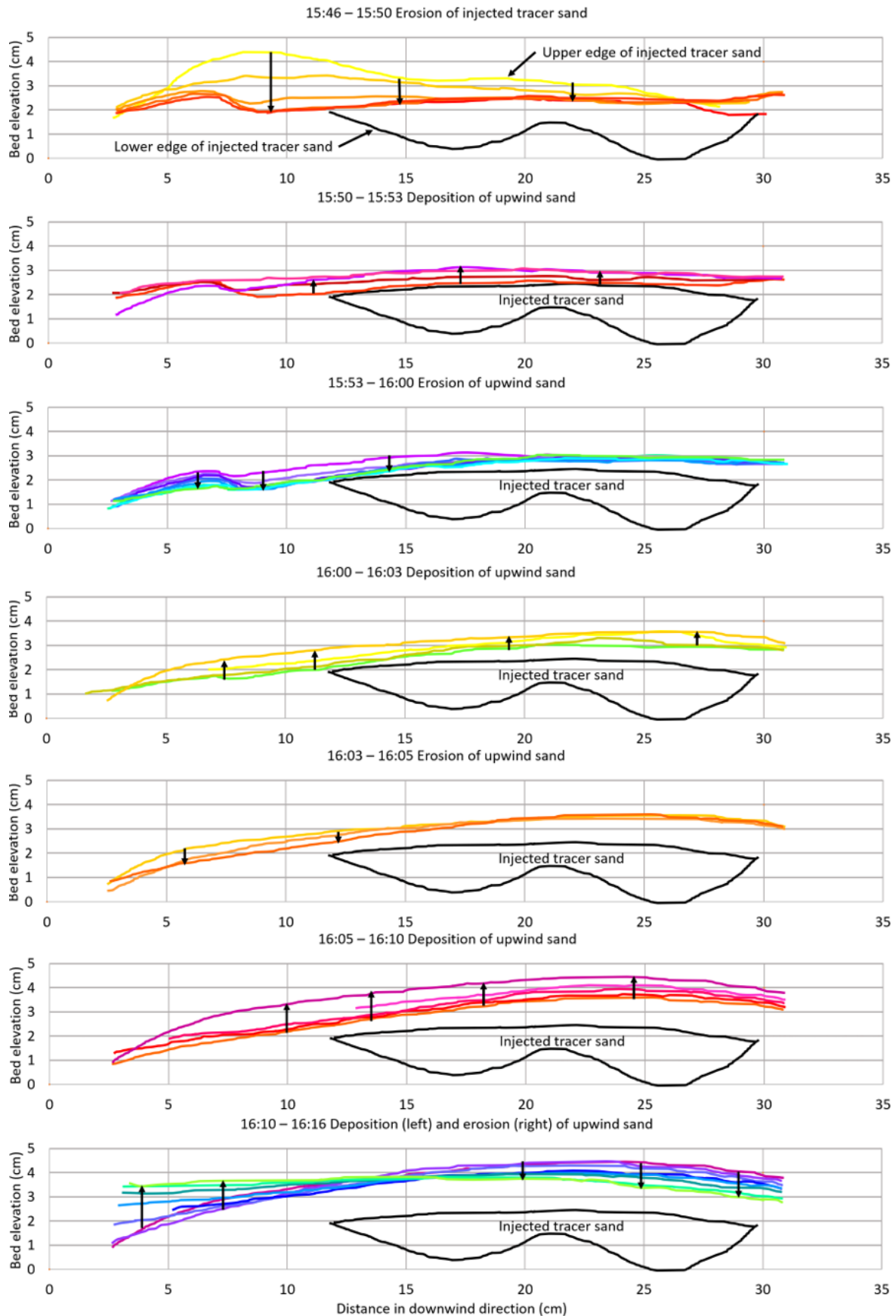


Figure 3.9: Bed elevation changes during S01 derived from digitized side view images. Wind was blowing from left to right. The first elevation is traced in yellow and then the elevation after every minute is shown in another color going from yellow, to red, to blue, to green, and back to yellow. During the first erosion phase (15:46 – 15:50), the placed tracer sand got partly eroded, then different phases of deposition (arrows facing upwards) and erosion (arrows facing downwards) of upwind sand alternated on top of the remaining tracer sand.

Conceptual model for an Active Bed Surface Layer

To interpret and to better understand the observed results, a conceptual model is developed and used to describe the dynamics in the interaction area between the bed and the moving air. The model aims to improve aeolian sediment transport predictions and models for beach areas between the intertidal zone and the dune toe of well-graded sandy beaches which are mainly exposed to winds with an onshore component.

4.1 Definition of an Active Bed Surface Layer (ABSL)

The results indicate that most of the sediment is transported near and at the bed. In the area near and the bed differently sized sand grains of the bed interact with the moving air of the wind and sediment sorting occurs. Additionally, erosion and deposition of upwind sand takes place near and at the bed. The dominant transport modes near and at the bed are creep and saltation, whereas the transport of grains in suspension takes place further away from the bed. Thus, we are mainly interested in the transport of grains in the form of creep and saltation, which are responsible for most of the transport. Modelling could benefit from defining a transport layer that accounts for this entire area where most sediment transport takes place and where the interaction between wind flow and sand particles takes place. To define this area we propose a new concept: the concept of an Active Bed Surface Layer (ABSL).

The ABSL includes the free movement of grains due to wind in the creep/saltation layer but also the mobile/erodible bed which characteristics impact the supply of sediment to the creep/saltation layer and which can show bed forms (Figure 4.1). Grains can dynamically change from the mobile bed to the creep/saltation layer and vice versa. The mobile bed takes into account both the horizontal movement of grains as bedload and the vertical movement of the sediment bed in the form of temporal erosion and deposition. To specify the boundaries of the ABSL, we define an upper and lower limit. The upper limit of the ABSL is the height to which the saltating particles reach (Figure 4.1). Martin and Kok (2017) found based on field observations that the aeolian saltation layer height is insensitive to variations in wind speed but is determined by the mean sand bed particle diameter (d_{50}). They found saltation heights in the order of 150 to 200 times d_{50} , which would imply saltation heights in the order centimeters for sand-sized particles.

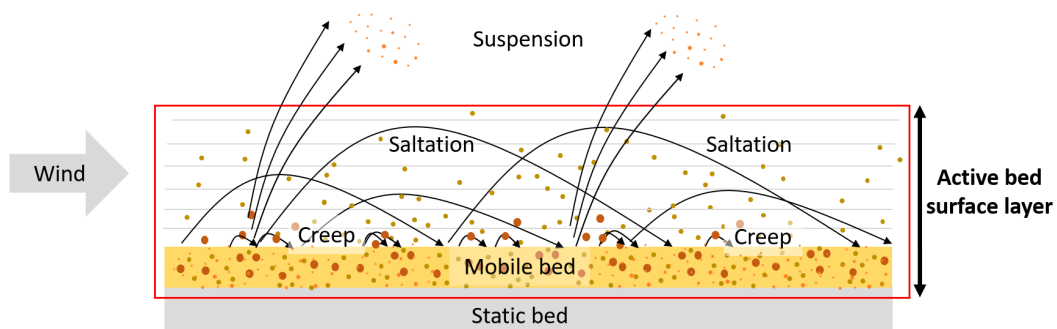


Figure 4.1: Schematic definition of the new concept: an Active Bed Surface Layer (ABSL) (inside red box). The ABSL is a zone where sand grains of different size (brown = coarsest grains, beige = medium grains) interact with the wind (streamlines are represented as light grey lines). It contains of a mobile bed and a creep/saltation layer above it. The lower limit of the ABSL is a static bed where no sediment transport takes place at any time.

The lower limit of the ABSL is a constant depth at which no sediment transport takes place at any time. This

means that there is a static bed under the mobile bed of the ABSL that does not get eroded at any time. The presence of such a static bed was observed for all experiments. The initially placed 3 cm thick tracer sand layer was never completely eroded from the placement site within the duration of the experiments (e.g., Figures 3.9 and 3.7). This implies that the depth at which no sediment transport takes place is in the order of centimetres below the upper edge of the moving bed.

Now that the boundaries of the ABSL are defined, the most important processes in this layer can be explored.

4.2 Sediment transport processes in the ABSL

The results indicate that for high wind conditions different horizontal and vertical transport processes of the four grain size fractions in the ABSL were present than for moderate wind conditions. Therefore, we define two transport regimes (I and II) with different movement characteristics of grains in the ABSL (Figure 4.2). The definition of the regimes is inspired by the research of Sherman et al. (2019) and Pye and Tsoar (2009). The regimes facilitate to relate the most important processes in the ABSL according to the tracer experiments and literature to their influence on the magnitude of aeolian sediment transport.

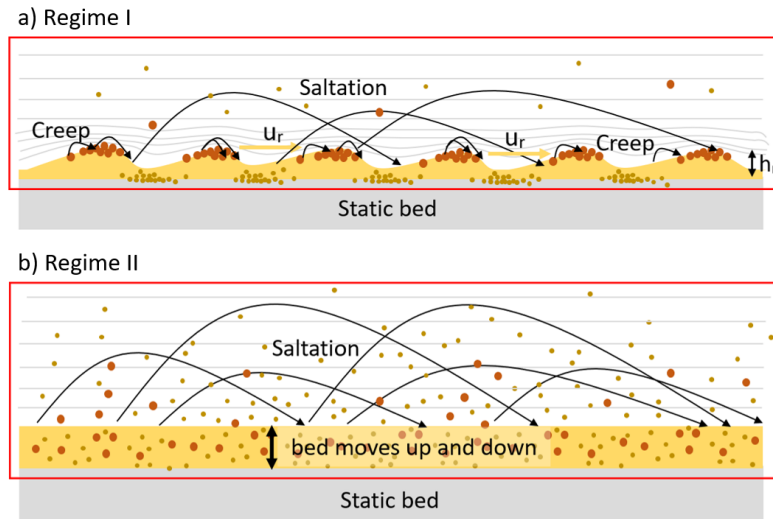


Figure 4.2: Schematic overview of the dynamics of the ABSL for the two regimes. a) For Regime I, ripples form as part of the ABSL (inside red square) with coarse grains (brown) at the ripple crests and finer grains (beige) in the ripple troughs. The ripples of height h_r move with a speed of u_r . Above the ripples, coarser grains mainly move in the form of creep, while finer grains mainly move in the form of saltation. b) For Regime II, upwind sediment temporarily deposits and erodes causing the mobile bed of the ABSL to move up and down. Above the mobile bed layer, both fine (beige) and coarse (brown) grains move in saltation.

To distinguish the two regimes, the dimensionless wind shear velocity u_*/u_{*t} is used which was earlier used by Sherman et al. (2019) in the context of aeolian ripple migration. This parameter incorporates both wind characteristics (u_*) and sediment characteristics (u_{*t}) and thus, enables to compare the findings of the tracer experiments with findings from literature and to place empirical findings from different studies in a more universal frame. The wind shear velocity, u_* , can be estimated from wind measurements by assuming a logarithmic profile and applying the Law of the Wall, see Equation 1.2. For the saltation induced roughness length, z'_0 , in Equation 1.2 different formulations exist. Based on a large data set of wind profile measurements, Sherman and Farrell (2008) compared the performance of different formulations and found that the Charnock (1955)-type model best replicated the data:

$$z'_0 = \frac{C u_*^2}{g} \quad (4.1)$$

where C is the Charnock constant with a value of 0.085 for general field applications and g is the gravity

constant. For estimating the threshold shear velocity, u_{*t} , the Bagnold (1935) model can be used:

$$u_{*t} = A \sqrt{gd \frac{\rho_s - \rho}{\rho}} \quad (4.2)$$

where A is an empirical constant (0.1 for the fluid threshold), ρ is air density (1.22 kg/m^3), and d is mean sand grain size (equal to d_{50}). When this threshold velocity is exceeded by the wind shear velocity, a small number of sand sized particles is lifted and saltation is initiated (van Rijn, 2019).

We define Regime I for $1 < u_*/u_{*t} \leq 4$ and Regime II for $u_*/u_{*t} > 4$ which corresponds to moderate and high wind speeds, respectively. The threshold of $u_*/u_{*t} = 4$ to distinguish Regime I from Regime II is based on the most important difference between the two regimes: the presence of ripples for Regime I and the absence of ripples for Regime II (Figure 4.2). According to Pye and Tsoar (2009), ripples disappear and a planar surface is formed when the threshold wind shear velocity is about three to four times the fluid threshold velocity. When $u_*/u_{*t} \leq 1$, no sand transport takes place in the ABSL. For Regime I, most transport in the ABSL takes place in close contact with the bed in the form of ripple movement, creep and saltation. Whereas for Regime II, most transport in the ABSL takes place in the form of saltation (Figure 4.2).

Once the mean grain size and the wind shear velocity are known, the regime can be determined according to Figure 4.3.

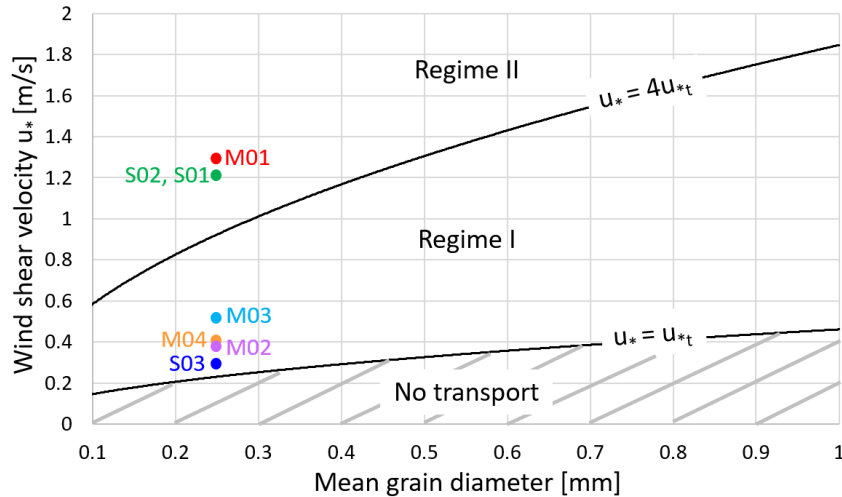


Figure 4.3: Regime classification based on mean grain size and wind shear velocity. The striped grey area underneath the $u_* = u_{*t}$ line corresponds to no transport in the ABSL, the area between the $u_* = u_{*t}$ and $u_* = 4u_{*t}$ line corresponds to Regime I, and the area above the $u_* = 4u_{*t}$ line corresponds to Regime II. The colored dots indicate in which regime the experiments M01 - M04 and S01 - S03 lie.

The two transport regimes are characterized by different dynamics in the ABSL due to different wind speeds, bed characteristics, and the supply of upwind sediment. These characteristics influence the magnitude of aeolian sediment transport in different ways and therefore require different modelling approaches, which will be shown in the following. The characteristics of the two regimes are described and suitable modelling approaches are suggested, for which the interpretation of our measurements is used.

4.2.1 Regime I

Characteristics

Experiments M02, M03, M04, and S03 fall in Regime I based on their dimensionless wind shear velocities u_*/u_{*t} (Figure 4.3). For M03, M04, and S03, ripples were present, which distinguishes Regime I events from Regime II events. The results of experiments M03, M04, and S03 indicate the following characteristics for Regime I:

- (1) Ripples form with coarser grains on the ripple crests and smaller grains in the ripples troughs (Figure 3.7).
- (2) Ripples propagate in downwind direction and a strong linear relationship between ripple propagation speed

and wind speed is present (Figure 3.6). (3) Once ripples have formed, the supply of finer grains in downwind direction decreases, while the supply of coarser grains stays constant (Figure 3.2).

Characteristic (1) is inline with literature about aeolian ripples. Bagnold (1954) was one of the first who explained the formation of aeolian ripples due to the instability of a flat bed. From observations, he found that a flat sand surface must be unstable when sand grains start to saltate because the rate of saltation impacts is higher on the windward than on the lee slopes of any small deformation of the bed surface. This explanation remains the basis of modern understanding of the initial stage of flat surface instability (Manukyan and Prigozhin, 2009). The subsequent formation of ripples and vertical sorting is often explained due to different transport trajectories of coarse and fine grains (Bagnold, 1954; Durán et al., 2011; Anderson and Bunas, 1993; Wang et al., 2019). Smaller grains tend to saltate over the crest and to reach the bottom, or beyond it, before coming to rest, whereas the larger grains tend to stop at the crests immediately (Bagnold, 1954).

Characteristic (2) is inline with Sherman et al. (2019). They compared ripple migration rates of their field studies (Jericoacoara, Brazil, 2009 and Oceano, California, 2015) to ripple migrations by Sharp (1963) and Andreotti et al. (2006) and also found a linear relationship between dimensionless shear velocity and ripple speed.

To the best of our knowledge, characteristic (3) has not yet been observed in the context of aeolian ripple sediment transport. The influence of ripples on the sediment supply for aeolian transport has not yet been investigated. Based on our results, we hypothesize that the formation of ripples in combination with vertical sorting processes causes the bed to be armored and therefore, the supply of sediment to be limited once ripples have formed. This hypothesis is based on the following considerations: The presence of the ripples at the bed can influence the streamlines of the wind close to the bed (Durán et al., 2011). At the ripple crests, the streamlines are likely to converge, which would cause the wind shear velocity to be maximum, whereas in the ripple troughs, the streamlines are likely to diverge, which would cause the wind shear velocity to be minimum (see light grey lines in Figure 4.4). At the ripple crests, where the wind shear stress is likely to be maximum, coarser grains are found (Figure 3.7). Within Regime I, wind shear velocities are relatively small and thus might be barely large enough to lift these coarser grains at the ripple crests in saltation. As a consequence, the coarser grains would mainly move as creep in near-continuous contact with the sand bed. At the ripple troughs, where the wind shear stress is likely to be minimum, finer grains are found (Figure 3.7). The finer grains in the troughs would be sheltered and only occasionally start saltating. This would mean that the combined effect of vertical sorting and the distortion of the wind stream lines due to the presence of ripples can cause Regime I situations to be supply-limited. Less sediment would be supplied from the moving bed into the creep/saltation layer compared to a situation with a well-mixed, flat bed. This hypothesis provides a possible explanation for characteristic (3). However, it is unclear to what extent ripples contribute to armoring and therefore to what extent they limit sediment supply for aeolian transport.

Sediment transport

For Regime I, ripples form as part of the mobile bed in the ABSL on top of an immobile, static bed (Figure 4.4). Sediment in the ABSL is partly transported as bedload in form of ripples, q_r , with the ripple velocity, u_r , and height, h_r , and partly transported in the layer above the ripples in the form of saltation, q_s . Besides that, it was observed that some individual grains moved as creep across ripple surfaces, q_c , faster than the ripples migrated. Therefore, the total sediment flux for Regime I can be written as:

$$q_I = q_r + q_s + q_c \quad (4.3)$$

In order to develop a sediment balance a control volume (red square, Figure 4.4) is used. During experiments M03 and M04, no significant bed level changes were observed. Thus, it is assumed that the vertical fluxes of erosion E and deposition D are small. As a consequence, all sediment that enters the control volume on the left-hand side leaves the control volume on the right-hand side: $q_{in} = q_{out} = q_I$. To make sediment transport predictions for this regime, the magnitude of this horizontal mass flux q_I needs to be known.

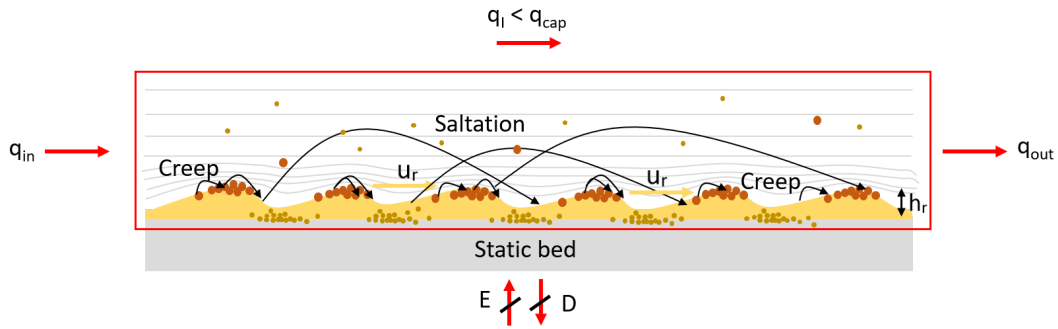


Figure 4.4: Schematic overview of the dynamics of the ABSL for Regime I. On top of a static bed (grey), ripples form as part of the ABSL (inside red square) with coarse grains (brown) at the ripple crests and finer grains (beige) in the ripple troughs. The ripples of height h_r move with a speed of u_r . Above the ripples, coarser grains mainly move in the form of creep, while finer grains mainly move in the form of saltation. The supply of bed sediment for saltation seems to be limited, causing the actual transport of Regime I to be smaller than the sediment transport capacity by wind, q_{cap} .

The mass of sand transported by ripple movement, q_r , can be estimated according to Jerolmack et al. (2006) as follows:

$$q_r = (1 - p)\rho_s u_r \frac{h_r}{2} \quad (4.4)$$

where p is porosity. Assuming that p , ρ_s , and h_r are constant, the magnitude of ripple sediment transport solely depends on the ripple speed. The strong linear relationship between wind speed and ripple speed (Figures 3.6) can be used to make accurate sediment transport predictions once the wind speed is known.

The second and third part of Equation 4.3 are the saltation and creep sediment fluxes q_s and q_c , respectively, which need to be determined. For this, we adopt the approach by Sherman et al. (2019) who related ripple transport rates to total sand transport rates. They found evidence that q_r/q_I increases weakly with shear velocity, indicating that the proportion of q_r relative to the total sediment transport q_I is nearly constant. With this information it is possible to relate ripple migration rates to total sand transport rates, once the proportion of ripple transport compared to total transport $X = q_r/q_I$ is known:

$$q_I = \frac{1}{X} q_r = \frac{1}{X} (1 - p)\rho_s u_r \frac{h_r}{2} \quad (4.5)$$

Sherman et al. (2019) found for their field studies that the proportion of ripple transport relative to the total transport averages $X = 0.036$. However, for this study, no sediment fluxes were measured to test the validity of that value and Sherman et al. (2019) even state that more field observations are needed to validate or refute the up-scaling relationship of Equation 4.5.

In the previous section we hypothesized based on characteristic (3) that the supply of sediment from the bed for saltation might be structurally limited for Regime I due to the armoring effect of ripples but we do not know to what extent. Generally, for supply-limited situations, the actual sediment transport is smaller than the theoretical sediment transport capacity by wind, q_{cap} , (Equation 1.3). Up-scaling ripple sediment transport rates, q_r , to total sediment transport rates, q_I , by using a constant factor, X , would imply that sediment transport is linearly proportional to wind speed. A linear relationship as Equation 4.5 is less powerful compared to a third power relationship describing the sediment transport capacity by wind, q_{cap} , (Equation 1.3) and could therefore be suitable to predict sediment transport rates under supply-limited conditions. Hence, we propose to use a linear relationship such as 4.5 to calculate aeolian sediment transport rates for Regime I, however, we are not able to verify this based on our field measurements.

4.2.2 Regime II

Characteristics

Experiments S01, M01, and S02 fall in Regime II based on their dimensionless wind shear velocities u_* / u_{*t} (Figure 4.3). For all three experiments no ripples were present. The results of the three experiments indicate

the following characteristics for Regime II: (1) Different grain size fractions do not show distinct differences in transport (Figure 3.3), indicating that grains of all sizes are moving in downwind direction. (2) Alternating phases of erosion and deposition of upwind sand are present (Figure 3.9) which cannot be explained by gradients in local wind speed only (Figure 3.8). (3) The magnitude of these erosion and deposition phases are of the same order (Figure 3.9), indicating that the average bed change on an hourly timescale is very small.

Characteristic (1) can be explained based on literature. According to Pye and Tsoar (2009), for Regime II wind velocities the ripples of Regime I disappear and a planar surface is formed. Wind velocities are high enough to bring the coarser grains, which accumulated at the ripple crests for Regime I, in saltation, causing the ripples to lengthen and flatten out. The ripple structure and also the armor layer are destroyed causing the smaller, sheltered particles to be available for sediment transport. Consequently, both finer and coarser grains are available for transport and no structural supply limitations are present. The dominant sediment transport mode is simultaneous saltation of finer and coarser grains (Figure 4.6).

Regarding characteristic (2), aeolian sediment transport models often account for changes in sediment transport due to changes in wind speed only. This implies that a temporal increase (decrease) in wind speed results in a temporal increase (decrease) in sediment transport, causing temporal erosion (deposition) of sediment. This is in contrast to characteristic (2). de Vries et al. (2013) and de Vries et al. (2014b) provide a possible explanation for characteristic (2). They related temporal variations in sediment transport fluxes not only to temporal changes in wind speed but also to temporal changes in upwind sediment supply. They found that spatially and temporally varying aeolian sediment transport can be modelled as a function of sediment supply and varying wind conditions resulting in phases of erosion and deposition. Temporal changes in upwind sediment supply can occur due to the presence of supply-limiting factors as described in the introduction.

By taking temporal changes of upwind sediment supply next to temporal variations in wind driven transport capacity into account, temporal bed level changes in the area between the intertidal zone and the dune toe can be explained according to Figure 4.5. In case the wind driven transport capacity increases temporally but upwind sediment supply increases to a smaller extent (E3) or even decreases (E1) due to upwind supply limitations, the area between the intertidal zone and the dune toe erodes temporally. Erosion can also occur when the wind driven transport capacity decreases (e.g., between 15:53 and 16:00, Figures 3.9 and 3.8) provided the upwind sediment supply decreases to a higher extent (E2). In any case, the depth to which the bed can erode is limited to the depth at which the non-erodible static bed begins. Temporal deposition, on the other hand, occurs for a temporally decreasing wind driven transport capacity and temporally increasing upwind sediment supply (D1) or temporally decreasing upwind sediment supply provided the decrease is smaller than the decrease in wind driven transport capacity (D3). Deposition is also possible when wind driven transport capacity increases (e.g., between 15:50 and 15:53, Figures 3.9 and 3.8) in case upwind sediment supply increases to a higher extent (D2). In case the upwind sediment supply increases (decreases) in a same way as the wind driven transport capacity, the bed level is constant.

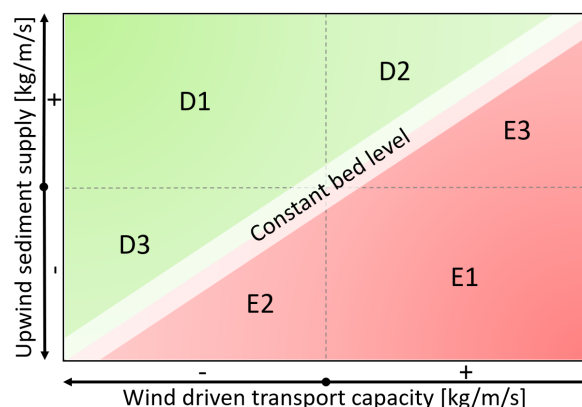


Figure 4.5: Temporal bed level changes in the area between the intertidal zone and the dune toe due to temporally increasing and decreasing wind driven sediment transport capacity and temporally increasing and decreasing upwind sediment supply. The green areas (D1 - D3) indicate different forms of temporal deposition and the red areas (E1 - E3) indicate different forms of temporal erosion. In case the upwind sediment supply increases (decreases) in a same way as the wind speed, the bed level is constant.

Consequently, the flux of upwind sediment influences whether the area between the intertidal zone and the dune toe is temporally eroding, accreting, or constant, and how much sediment is transported. The properties of the bed surface sediment in this area itself seem to be of minor importance. Moreover, the temporal average of these erosion and accretion phases appears to be very small on an hourly time scale (characteristic (3)). This means that no sediment is taken or added from the area between the intertidal zone and the dune toe, indicating that this area cannot be the source for the observed sediment flux. It is more likely that the transported sediment is eroded from upwind areas (which would be the intertidal zone for winds with an onshore component) and that the considered area functions as a pathway for sediment eroded from these areas.

Sediment transport

For Regime II, upwind sediment temporarily deposits and erodes on top of an immobile, static bed, causing the mobile bed of the ABSL to move up and down in the order of centimeters (Figure 4.6). This is the consequence of a difference in sediment transport at the incoming and outgoing side of the control volume (red square in Figure 4.6). In case $q_{in} < q_{out}$ sediment erodes from the test site ($E - D > 0$) and in case $q_{in} > q_{out}$ sediment accretes on the test site ($E - D < 0$). For $q_{in} = q_{out}$ the bed is constant.

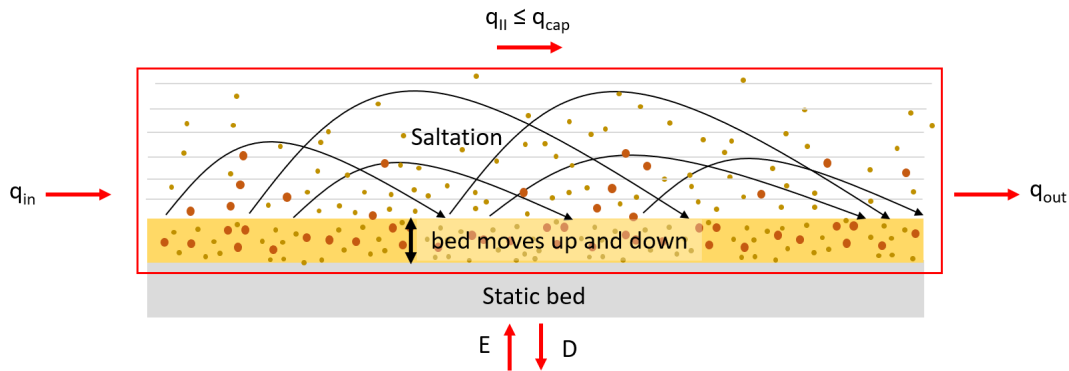


Figure 4.6: Schematic overview of the dynamics of the ABSL for Regime II. On top of a static bed (grey), upwind sediment temporarily deposits (D) and erodes (E) causing the mobile bed of the ABSL to move up and down in the order of centimeters. Above the mobile bed layer, both fine (beige) and coarse (brown) grains move in saltation.

For Regime II, the wind shear velocity is sufficiently high so that both coarse and fine grains are transported in saltation. To make sediment transport predictions for this regime, the magnitude of the horizontal mass flux needs to be known which depends on variations in wind speed and upwind sediment supply. In case of temporal deposition (D1 - D3, Figure 4.5), the particle concentration in the saltation layer is too high for the prevailing wind speed, so that a certain amount of sand leaves the saltation layer in form of deposition in the ABSL. In this case, the sediment flux is temporally (over-)saturated, which means that the transport capacity by wind is reached: $q_{II} = q_{cap}$. To estimate the magnitude of the sediment transport capacity, q_{cap} , the third power relation by Bagnold (1937) (Equation 1.3) could for instance be used.

In case of temporal erosion (E1 - E3), the sediment flux is temporally not saturated due to upwind supply limitations or spatiotemporal variations in wind speed ($q_{II} < q_{cap}$). The particle concentration in the saltation layer is too small for the prevailing wind speed, so that additional sediment from the mobile bed is added in form of erosion in the ABSL. To account for spatiotemporal variations in wind speed and supply limitations, we suggest to use Equation 1.3 within a process-based area model such as AeoliS (Hoonhout and Vries, 2016) that simulates spatiotemporal variations in bed surface properties and sediment availability for the entire beach area.

Discussion

We explored the concept of an Active Bed Surface Layer (ABSL) that can help to model aeolian sediment transport as a function of wind speed, sediment supply and bed characteristics such as grain size and bedforms. The model is based on our findings on the horizontal and vertical movement of differently sized grains in the interaction zone between the bed and the moving air, obtained through our novel fieldwork method using tracers in a small-scale coastal beach environment, microscopic analysis of the tracer samples and additions from the literature. The conceptual model differentiates between two regimes for different transport characteristics in the ABSL and proposes different modelling approaches for these two regimes to estimate the magnitude of aeolian sediment transport in supply-limited coastal environments.

To differentiate between the two regimes of the conceptual model, the dimensionless wind shear velocity, u_*/u_{*t} , accounting for wind speed variations measured at various heights (through u_*) and different grain sizes (through u_{*t}) is introduced. This dimensionless parameter has the advantage of being able to compare the findings of this study to other studies, and to enable future research to place new empirical findings in the framework of our conceptual model. On the other hand, it has the disadvantage that it can generate conceptual errors through idealizations/assumptions in the data interpretation equations of the wind shear velocity, u_* , and the wind shear threshold velocity, u_{*t} . The formulation of the wind shear velocity for instance uses the 'Law of the Wall' which assumes a vertical logarithmic velocity profile. Wind measurements in the field, however, often deviate from a stable logarithmic velocity profile which brings uncertainty in estimating wind shear velocity u_* from wind measurements at a certain height u_w when applying the 'Law of the Wall' (Bauer et al., 1992).

The conceptual model with its different regimes was developed based on certain environmental conditions that were present on the beach in Noordwijk (grain size, wind speed and direction, moisture, beach characteristics) and for one specific area (between the intertidal zone and the dune toe) and is supported by literature. The model accounts for variability in grain size and wind speed by using the dimensionless wind shear velocity. However, it does not account for all relevant physics influencing the characteristics of the ABSL (e.g., moisture, beach width and slope, vegetation). Future research should explore the influence of more physical parameters on the characteristics of the ABSL by performing similar tracer experiments as done for this study. The new insights could help to extend the framework of the conceptual model by adding new regimes and/or adjust the Bagnold (1935) threshold velocity formulation. For example, moisture could increase the threshold velocity and thus influence the regime boundaries. Furthermore, moisture could also affect the bed characteristics. Nield et al. (2011) found that after rainfall, adhesion structures instead of ripples developed on a drying beach which were much larger than ripples. Due to their different dimensions, they might influence aeolian sediment transport differently than ripples. To implement this different behavior in the model, a new regime could be developed.

Our novel definition of the ABSL includes the entire area where most sediment transport takes place: the mobile/erodible bed and the creep/saltation layer. Sediment in the ABSL moves in horizontal and vertical direction under the influence of wind speed variations, upwind sediment supply, and bed characteristics. Existing numerical area models such as the one by Hoonhout and Vries (2016) or Durán and Moore (2013) do not account for complex interactions between the sediment bed and the wind. This can lead, for example, to the calculation of unrealistically large erosion depths or to the neglect of the possibly supply-limiting effect of bedforms. To improve the prediction quality of future numerical area models, modelers should focus on a better discretization of the interaction area between the moving air and the sediment bed by applying our new concept of an ABSL.

We defined the bottom boundary of the ABSL as the interface between the moving bed and the static bed. The moving bed represents the short-term variability of bed level changes in the order of centimetres that we observed on a time scale of minutes. One could conclude that these bed level changes of centimeters add up to bed level changes of decimeters or meters for longer time periods. However, we could observe on an hourly time scale that average bed level changes were very small. This is in accordance with the findings of de Vries et al. (2015) who observed limited bed level changes in the upper area of Dutch beaches under aeolian forcing on the time scale

of years. To account for this limited long-term variability in our model, we defined a static, non-erodible layer underneath the mobile layer. However, our model description lacks a quantitative definition at which vertical distance this static bed begins. To find a quantitative description for this vertical distance, future research should investigate the applicability of hydrodynamic concepts for aeolian environments that define a vertical limit to bed movement based on physical or modelling considerations, such as the Depth of Disturbance (DoD) concept of King (1951) or the Sediment Layers with source-sink Exchange (SILKE) concept of Chavarrias et al. (2019), respectively.

The proposed linear relationship between sediment transport and wind speed for Regime I events is based on the idea of upscaling the linear relationship between ripple speed and wind speed. We could find a strong linear relationship between ripple speed and wind speed for the experiments M03 and M04 (Figure 3.7). Sherman et al. (2019) compared ripple migration rates of their field studies (Jericoacoara, Brazil, 2009 and Oceano, California, 2015) to ripple migrations by Sharp (1963) and Andreotti et al. (2006) and also found a linear relationship between dimensionless shear velocity and ripple speed. We transferred our results of measured ripple speed u_r and wind speed u_w to the dimensionless parameters u_r/\sqrt{gd} and u_*/u_{*t} suggested by Sherman et al. (2019) and compared it to their data that fell in Regime I (Figure 5.1). Performing linear regression analysis for all data ($u_r/\sqrt{gd} = 0.004u_*/u_{*t} - 0.0032$ with $n = 207$ and $R^2 = 0.47$) and just our data ($u_r/\sqrt{gd} = 0.0049u_*/u_{*t} - 0.0072$ with $n = 46$ and $R^2 = 0.86$) shows that the slope of the relationship is almost the same, which indicates that the data from our study are consistent with the relationship by Sherman et al. (2019).

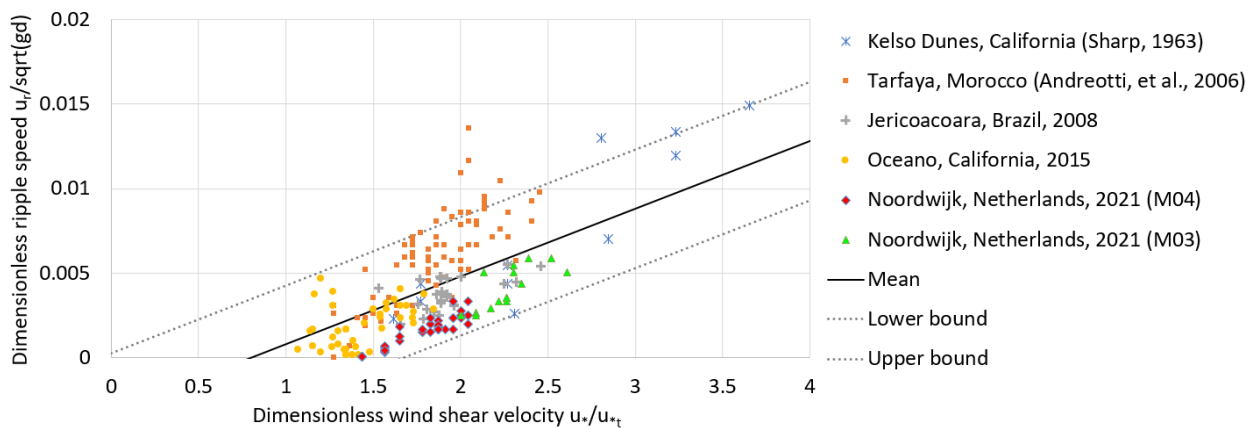


Figure 5.1: Dimensionless migration rates as a function of dimensionless shear velocity ($n = 207$, $R^2 = 0.47$). The solid line indicates the mean through all measurement points, the dashed lines indicate the 10%-quantile. For 10% of the measurements, the dimensionless ripple speed u_r/\sqrt{gd} deviates more than 0.0032 from the mean value.

Aeolian process measurements generally lack a standardized method to compare measurements from one study to another (Barchyn et al., 2011). The most common methods to measure aeolian sediment transport are sediment traps, and optical and acoustic backscatter which are all point measurement methods (Black et al., 2017; White, 1998). Among these point measurement methods, there is no standardised way how to set up the measurement instruments (e.g., at which height to place a sediment trap, at what frequency to measure) or how to derive sediment fluxes from the measurements. This makes it difficult to compare between studies and to assess results quantitatively rather than qualitatively (Barchyn et al., 2011). For this study we performed particle tracing, which is different compared to point measurements because it focuses on the spatiotemporal dispersal of the tracer rather than the sediment flux at one point. This method enabled us to investigate the transport rates of different grain size fractions relative to the total transport of all grain size fractions in a qualitative way. We considered carrying out point measurements in addition to particle tracking in order to obtain more quantitative measurement results. However, due to the lack of standardisation, point measurements would also only have provided further qualitative insight into sediment transport instead of quantitative.

Consequently, the conceptual model developed here is supported by the findings of our field measurements using tracers. Based on our findings and additions from literature, we developed a sediment balance for the

different regimes and proposed transport formulations. We did not validate or calibrate the proposed transport formulations by point measurements of sediment fluxes because of the lack of a standardized method. This means that our confidence in the proposed transport formulations is limited to the significant difference between 'a lot of' transport during Regime II and 'less' transport during Regime I. However, based on the insights we gained from the conceptual model, it can help to better quantify aeolian sediment transport in the future by focusing on the most important processes in the ABSL and by using different transport regimes for different wind speeds. Future research should focus on establishing a standard method for measuring aeolian sediment transport processes to overcome comparison problems between different studies and to allow a more quantitative interpretation of measurement results.

Conclusions

In this study, we analyzed the horizontal and vertical transport of differently sized grains in the interaction area between the moving air and the sediment bed by conducting fieldwork using differently colored tracers according to particle size. Seven experiments were conducted in the area between the intertidal zone and the dune toe at a well-graded sandy beach in Noordwijk, Netherlands, for varying wind speeds with an onshore component. Cameras and sediment sampling were used to track the sediment movement on the bed surface. Wind speed and direction were measured to relate the findings to the concurrent environmental conditions.

The results show that for moderate wind conditions, the tracer sand interacted with the sediment entering the test site from the upwind direction, forming aeolian ripples with coarser grains on the ripple crests and smaller grains in the ripples troughs. Once the ripples have formed, the supply of finer tracer grains in the downwind direction decreased over time, while the supply of coarser grains remained constant. A strong linear relationship between ripple propagation speed and wind speed was found. For higher wind velocities, no ripples or differences in transport of different grain sizes in downwind direction were observed. Temporal phases of erosion and deposition of up to 2 cm upwind sand were observed which could not be related to local gradients in wind speed.

Based on these results and with additions from literature, we developed a conceptual model for an Active Bed Surface Layer (ABSL) that can help to describe coastal aeolian sediment transport as a function of wind speed, sediment supply, and bed characteristics. The most important characteristics of the ABSL were explained for two transport regimes corresponding to moderate (I) and high (II) wind speeds. The characteristics of the ABSL were further used to investigate how they influence the magnitude of aeolian sediment transport for the regimes. The dimensionless wind shear velocity defined as the ratio of wind shear velocity, u_* , over wind shear threshold velocity, u_{*t} , is used to distinguish between the regimes. The most important findings for the two regimes are:

- For Regime I ($1 < u_*/u_{*t} \leq 4$) ripples form as part of the ABSL. The combination of coarser grains at the ripple crest where wind speed is maximum and finer grains in the ripple troughs where wind speed is minimum seems to limit the supply of bed sediment for saltation. Sediment is partly transported as bedload in the form of ripples, which scales linearly with wind speed, and partly transported above the bed in the form of creep and saltation. It might be possible to upscale the linear relationship between ripple transport and wind speed to make total sediment transport predictions for Regime I by using a constant value for the proportion of ripple transport compared to total transport according to Sherman et al. (2019). This would mean that total sediment transport is linearly proportional to wind speed, which is less strong than a third power relationship for aeolian sediment transport capacity and therefore seems appropriate for a structurally supply limited situation.
- The dynamics of the ABSL of Regime II ($u_*/u_{*t} > 4$) are mainly influenced by the supply of upwind sediment and spatiotemporal variations in wind speed. Temporal varying gradients in upwind sediment supply and wind speed can result in temporal phases of erosion and deposition. A third power relationship between sediment transport and wind speed in combination with a process-based model that accounts for supply limitations seems suitable for making aeolian sediment transport predictions for Regime II. The time average of the eroding and accreting phases seems to be very small which indicates that the considered beach area functions as a pathway for sediment eroded from upwind areas rather than as a source for aeolian sediment itself.

The conceptual model for the ABSL is supported by the findings of our field measurements. It can help to improve numerical area models and to better quantify aeolian sediment transport in the future by focusing on the most important processes in the ABSL and by using different transport regimes for different wind speeds.

Bibliography

- Anderson, R. and Bunas, K. (1993). Grain size segregation and stratigraphy in aeolian ripples modelled with a cellular automaton. *Nature*, 365(6448):740–743.
- Andreotti, B., Claudin, P., and Pouliquen, O. (2006). Aeolian sand ripples: Experimental study of fully developed states. *Phys. Rev. Lett.*, 96:028001.
- Bagnold, R. A. (1935). The movement of desert sand. *The Geographical Journal*, 85(4):342–365.
- Bagnold, R. A. (1937). The transport of sand by wind. *The Geographical Journal*, 89(5):409–438.
- Bagnold, R. A. (1954). *The Physics of Blown Sand and Desert Dunes*. Dover Publications, INC.
- Barchyn, T. E., Hugenholtz, C. H., and Ellis, J. T. (2011). A call for standardization of aeolian process measurements: moving beyond relative case studies. *Earth Surface Processes and Landforms*, 36(5):702–705.
- Barchyn, T. E., Martin, R. L., Kok, J. F., and Hugenholtz, C. H. (2014). Fundamental mismatches between measurements and models in aeolian sediment transport prediction: The role of small-scale variability. *Aeolian Research*, 15:245–251.
- Bauer, B. O. and Davidson-Arnott, R. G. (2003). A general framework for modeling sediment supply to coastal dunes including wind angle, beach geometry, and fetch effects. *Geomorphology*, 49(1):89–108.
- Bauer, B. O., Sherman, D. J., and Wolcott, J. F. (1992). Sources of uncertainty in shear stress and roughness length estimates derived from velocity profiles. *The Professional Geographer*, 44(4):453–464.
- Berg, N. H. (1983). Field evaluation of some sand transport models. *Earth Surface Processes and Landforms*, 8(2):101–114.
- Black, K., Athey, S., Wilson, P., and Evans, D. (2007). The use of particle tracking in sediment transport studies: A review. *Geological Society, London, Special Publications*, 274:73–91.
- Black, K., Poleykett, J., Uncles, R. J., and Wright, M. R. (2017). *Sediment Transport: Instrumentation and Methodologies*, pages 261–292.
- Blom, A. (2003). *A vertical sorting model for rivers with non-uniform sediment and dunes*. PhD thesis, Universiteit Twente, Veenendaal, the Netherlands.
- Buckley, R. (1987). The effect of sparse vegetation on the transport of dune sand by wind. *Nature*, 325(6103):426–428.
- Cabrera, L. L. and Alonso, I. (2010). Correlation of aeolian sediment transport measured by sand traps and fluorescent tracers. *Journal of Marine Systems*, 80(3):235–242. Models and observations of Marine Systems.
- Charnock, H. (1955). Wind stress on a water surface. *Quarterly Journal of the Royal Meteorological Society*, 81(350):639–640.
- Chavarrías, V., Arkesteijn, L., and Blom, A. (2019). A well-posed alternative to the hirano active layer model for rivers with mixed-size sediment. *Journal of Geophysical Research: Earth Surface*, 124(11):2491–2520.
- Davidson-Arnott, R. G., MacQuarrie, K., and Aagaard, T. (2005). The effect of wind gusts, moisture content and fetch length on sand transport on a beach. *Geomorphology*, 68(1):115–129. Fluid Flow and Sediment Transport Process in Geomorphology.
- de Vries, S., Arens, S., de Schipper, M., and Ranasinghe, R. (2014a). Aeolian sediment transport on a beach with a varying sediment supply. *Aeolian Research*, 15:235–244.
- de Vries, S., Harley, M. D., de Schipper, M. A., and Ruessink, G. (2015). *Dune growth due to aeolian sediment transport and the role of the beach and the intertidal zone*.

- de Vries, S., Southgate, H., Kanning, W., and Ranasinghe, R. (2012). Dune behavior and aeolian transport on decadal timescales. *Coastal Engineering*, 67:41–53.
- de Vries, S., van Thiel de Vries, J., and Ruessink, G. (2013). Modelling aeolian sediment accumulations on a beach.
- de Vries, S., van Thiel de Vries, J., van Rijn, L., Arens, S., and Ranasinghe, R. (2014b). Aeolian sediment transport in supply limited situations. *Aeolian Research*, 12:75–85.
- Durán, O. and Moore, L. J. (2013). Vegetation controls on the maximum size of coastal dunes. *Proceedings of the National Academy of Sciences*, 110(43):17217–17222.
- Durán, O., Claudin, P., and Andreotti, B. (2011). On aeolian transport: Grain-scale interactions, dynamical mechanisms and scaling laws. *Aeolian Research*, 3(3):243–270.
- Hardisty, J. and Whitehouse, R. (1988). Evidence for a new sand transport process from experiments on saharan dunes. *Nature*, 332(6164):532–534.
- Hesp, P., Network, C. D. V., and Institute, N. Z. F. R. (2000). *Coastal Sand Dunes: Form and Function*. CDVN technical bulletin. Forest Research.
- Hoonhout, B. and de Vries, S. (2017). Field measurements on spatial variations in aeolian sediment availability at the sand motor mega nourishment. *Aeolian Research*, 24:93–104.
- Hoonhout, B. and Vries, S. (2016). A process-based model for aeolian sediment transport and spatiotemporal varying sediment availability. *Journal of Geophysical Research: Earth Surface*, 121.
- Houser, C. (2009). Synchronization of transport and supply in beach-dune interaction. *Progress in Physical Geography*, 33:733–746.
- Hsu, S.-A. (1971). Wind stress criteria in eolian sand transport. *Journal of Geophysical Research (1896-1977)*, 76(36):8684–8686.
- Jerolmack, D. J., Mohrig, D., Grotzinger, J. P., Fike, D. A., and Watters, W. A. (2006). Spatial grain size sorting in eolian ripples and estimation of wind conditions on planetary surfaces: Application to meridiani planum, mars. *Journal of Geophysical Research: Planets*, 111(E12).
- Kato, S., Okabe, T., Aoki, Y., and Kamohara, S. (2014). Field measurement of sand movement on river-mouth tidal flat using color sand tracing. *Coastal Engineering Proceedings*, 1(34):sediment.61.
- Kawamura, R. (1951). Study on sand movement by wind.
- Keyence Corporation (2014). *VHX-5000 Digital Microscope User's Manual*. Keyence Corporation.
- King, C. A. M. (1951). Depth of disturbance of sand on sea beaches by waves. *Journal of Sedimentary Research*, 21(3):131–140.
- Kroon, A. and Hoekstra, P. (1990). Eolian sediment transport on a natural beach. *Journal of Coastal Research*, 6(2):367–379.
- Lettau, K. and Lettau, H. (1978). *Experimental and micrometeorological field studies of dune migration*, page 110–147. IES Report 101.
- Manukyan, E. and Prigozhin, L. (2009). Formation of aeolian ripples and sand sorting. *Physical review. E, Statistical, nonlinear, and soft matter physics*, 79:031303.
- Martin, R. and Kok, J. (2017). Wind-invariant saltation heights imply linear scaling of aeolian saltation flux with shear stress. *Science Advances*, 3.
- Nickling, W. and Davidson-Arnott, R. (1990). Aeolian sediment transport on beaches and coastal sand dunes.
- Nield, J. M., Wiggs, G. F., and Squirrell, R. S. (2011). Aeolian sand strip mobility and protodune development on a drying beach: examining surface moisture and surface roughness patterns measured by terrestrial laser scanning. *Earth Surface Processes and Landforms*, 36(4):513–522.

- Oliveira, S., Moura, D., Horta, J., Nascimento, A., Gomes, A., and Veiga-Pires, C. (2017). The morphosedimentary behaviour of a headland–beach system: Quantifying sediment transport using fluorescent tracers. *Marine Geology*, 388:62–73.
- Owen, P. (1964). Saltation of uniform grains in air. *Journal of Fluid Mechanics* 20, pages 225–242.
- Pähtz, T., Parteli, E. J. R., Kok, J. F., and Herrmann, H. J. (2014). Analytical model for flux saturation in sediment transport. *Phys. Rev. E*, 89:052213.
- Parker, G. (2008). *Transport of Gravel and Sediment Mixtures*, pages 165–252. ASCE Manuals and Reports on Engineering Practice No. 110.
- Pearson, S. G., van Prooijen, B. C., Poleykett, J., Wright, M., Black, K., and Wang, Z. B. (2021). Tracking fluorescent and ferrimagnetic sediment tracers on an energetic ebb-tidal delta to monitor grain size-selective dispersal. *Ocean and Coastal Management*.
- Pye, K. and Tsoar, H. (2009). *Aeolian Bed Forms*, pages 175–253. Springer Berlin Heidelberg, Berlin, Heidelberg.
- Quartel, S., Ruessink, B. G., and Kroon, A. (2007). Daily to seasonal cross-shore behaviour of quasi-persistent intertidal beach morphology. *Earth Surface Processes and Landforms*, 32(9):1293–1307.
- Robin, N., Levoy, F., and Monfort, O. (2009). Short term morphodynamics of an intertidal bar on megatidal ebb delta. *Marine Geology*, 260(1):102–120.
- Sarre, R. (1989). Aeolian sand drift from the intertidal zone on a temperate beach: Potential and actual rates. *Earth Surface Processes and Landforms*, 14(3):247–258.
- Schmutz, P. P. and Namikas, S. L. (2018). Measurement and modeling of the spatiotemporal dynamics of beach surface moisture content. *Aeolian Research*, 34:35–48.
- Sharp, R. P. (1963). Wind ripples. *The Journal of Geology*, 71(5):617–636.
- Sherman, D. and Hotta, S. (1990). *Aeolian sediment transport: theory and measurement*, pages 18–37. John Wiley & Sons, LTD.
- Sherman, D. J. and Farrell, E. J. (2008). Aerodynamic roughness lengths over movable beds: Comparison of wind tunnel and field data. *Journal of Geophysical Research: Earth Surface*, 113(F2).
- Sherman, D. J., Jackson, D. W., Namikas, S. L., and Wang, J. (1998). Wind-blown sand on beaches: an evaluation of models. *Geomorphology*, 22(2):113–133. Aeolian Environments.
- Sherman, D. J. and Li, B. (2012). Predicting aeolian sand transport rates: A reevaluation of models. *Aeolian Research*, 3(4):371–378. The 7th International Conference on Aeolian Research (ICAR VII), Santa Rosa, Argentina.
- Sherman, D. J., Li, B., Ellis, J. T., Farrell, E. J., Maia, L. P., and Granja, H. (2013). Recalibrating aeolian sand transport models. *Earth Surface Processes and Landforms*, 38(2):169–178.
- Sherman, D. J., Zhang, P., Martin, R. L., Ellis, J. T., Kok, J. F., Farrell, E. J., and Li, B. (2019). Aeolian ripple migration and associated creep transport rates. *Geosciences*, 9(9).
- Silva, A., Taborda, R., Rodrigues, A., Duarte, J., and Cascalho, J. (2007). Longshore drift estimation using fluorescent tracers: New insights from an experiment at comporta beach, portugal. *Marine Geology*, 240:137–150.
- Sutherland, T., Lane, P., Amos, C., and Downing, J. (2000). The calibration of optical backscatter sensors for suspended sediment of varying darkness levels. *Marine Geology*, 162(2):587–597.
- Sørensen, M. (2004). On the rate of aeolian sand transport. *Geomorphology*, 59(1):53–62. Aeolian Research: processes, instrumentation, landforms and palaeoenvironments.
- van der Wal, D. (1998). Effects of fetch and surface texture on aeolian sand transport on two nourished beaches. *Journal of Arid Environments*, 39(3):533–547.
- van Rijn, L. C. (2019). Aeolian transport over a flat sediment surface.

- Vila-Concejo, A., Óscar Ferreira, Ciavola, P., Matias, A., and Dias, J. M. (2004). Tracer studies on the updrift margin of a complex inlet system. *Marine Geology*, 208(1):43–72.
- Walker, J. (1981). An Experimental Study of Wind Ripples. Master's thesis, Massachusetts Institute of Technology, Cambridge, MA, USA.
- Walstra, D., Reniers, A., Ranasinghe, R., Roelvink, J., and Ruessink, B. (2012). On bar growth and decay during interannual net offshore migration. *Coastal Engineering*, 60:190–200.
- Wang, G., Li, J., Ravi, S., Scott Van Pelt, R., Costa, P. J., and Dukes, D. (2017). Tracer techniques in aeolian research: Approaches, applications, and challenges. *Earth-Science Reviews*, 170:1–16.
- Wang, P., Zhang, J., and Huang, N. (2019). A theoretical model for aeolian polydisperse-sand ripples. *Geomorphology*, 335:28–36.
- White, T. E. (1998). Status of measurement techniques for coastal sediment transport. *Coastal Engineering*, 35(1):17–45.
- Wijnberg, K. M. and Terwindt, J. H. (1995). Extracting decadal morphological behaviour from high-resolution, long-term bathymetric surveys along the holland coast using eigenfunction analysis. *Marine Geology*, 126(1):301–330.
- Williams, J. J., O'Connor, B. A., Arens, S. M., Abadie, S., Bell, P., Balouin, Y., Boxel, J. H. V., Carmo, A. J. D., Davidson, M., Ferreira, O., Heron, M., Howa, H., Hughes, Z., Kaczmarek, L. M., Kim, H., Morris, B., Nicholson, J., Pan, S., Salles, P., Silva, A., Smith, J., Soares, C., and Vila-Concejo, A. (2003). Tidal inlet function: Field evidence and numerical simulation in the india project. *Journal of Coastal Research*, 19(1):189–211.
- Wright, M., Poleykett, J., and Black, K. (2015). P1486.03.05.d01v92 - scarborough south bay sand tracking (final report), partrac.
- Zingg, A. (1953). Wind tunnel studies of the movement of sedimentary material. In: Proceedings, 5th Hydraulics Conference, Studies in Engineering.



Additional information

Preliminary tests

A.1 Initial research objective

Initially, the goal of this project was to observe the transport pathways and transport modes of tracer particles in the intertidal/swash zone, on the dry beach and in the dunes. The goal was to prove the hypothesis that marine sediment accumulation/aeolian sediment erosion in the swash zone is the main driving factor for dune growth.

The idea was to place fluorescent tracer sediment of about 1 m x 1 m with a thickness of a few centimeters at different areas of the beach. To observe sediment transport pathways, samples at different distances away from the tracer site should have been taken. To observe sediment transport modes, GoPro cameras from the side and top view should have been taken.

From first tests on the beach however, it turned out that both ideas need improvement and/or are not feasible within this project.

A.2 Test 01

The aim of the first test is to test

- different heights for the top view GoPro camera,
- the feasibility of a side view camera with a black screen in the background,
- screens with sticky foil to catch transported sediment,
- and the implementation of 1 m^2 tracer sand in the intertidal zone incl. moisture content.

For testing different heights of the top view GoPro camera, pictures from different distances above ground are taken.

For the side view camera, a black screen is placed and videos from different distance away from it, while throwing sand in the picture, are taken. The wind was not blowing strong enough, therefore, sand was thrown to assess the visibility of moving sand in front of the black screen.

Cardboard screens with sticky foil of 20 cm x 20 cm are used to catch transported sediment close to the ground. They are aligned perpendicular to the wind direction.

The colored sand is implemented in the intertidal zone just after high tide. Small wood sticks are used to mark the 1 m^2 injection site and a wood plate is taken to protect the sand from getting blown away during the implementation. A shovel is used to remove a thin layer of native sediment, then the colored sand is placed.

To create a moisture content of the tracer sand that mimics the native sand, a bucket of sea water is poured over one corner of the test site (left image, figure A.1). The wet corner with the sea water seems to be wetter than the native sand in the area, which already started drying after the high tide. On the other hand, the remaining sand seems to be much dryer than the surrounding sand.

After the wind was blowing for about 5 minutes, most of the red tracer sand got eroded (right image, figure A.1). It is clearly visible that the wet parts of the injection site got eroded less. This shows that the moisture content influences the transport behaviour significantly and thus, it is important to replicate it properly.

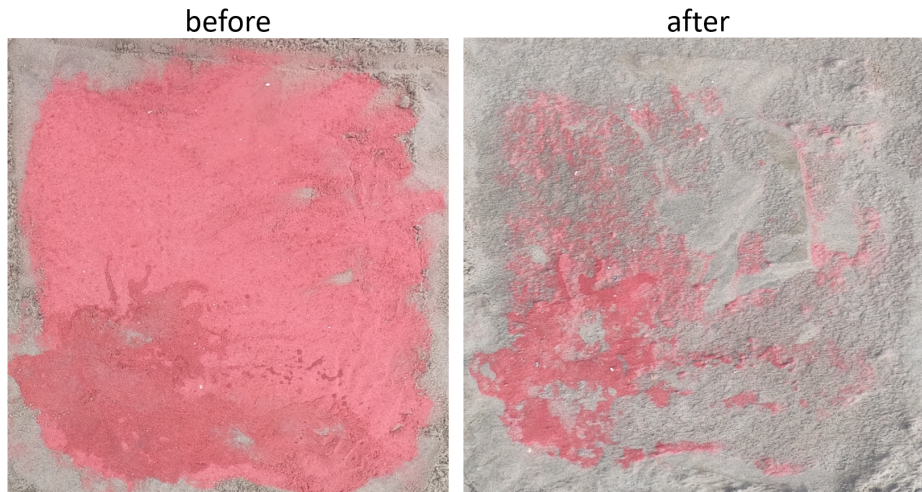


Figure A.1: Left: 1 m^2 test site with red sand after injection. Sea water was poured over the low left corner to create a moisture content. Right: Eroded test site after the wind has blown some tracer sand away. The wet, low left corner got eroded less.

A.2.1 Conclusions Test 01

From testing different heights it turned out that for a height of 50 cm above ground, almost the whole 1 m^2 test site can be observed and the image is sharp. For heights closer to the ground (10 cm and less), the GoPro images begin to blur and the camera loses focus.

A black screen in the background of the site view videos provides a good contrast and makes the white and colored particles more visible.

The screens with sticky foil are suitable to catch sediment when aligned perpendicular to the wind direction. However, this set up influences the wind field. A less intrusive alignment could be to have the sticky screens just under a small angle with the wind direction.

The above mentioned placing method is feasible and will be kept for further experiments.

Creating a moisture content of the tracer sand that mimics the native sand is quite challenging.

A.3 Test 02

After test 01 and while thinking of a set up for test 02, it turned out that observing the sediment transport pathways and observing the dynamics of the injection site are two different experiments, requiring two different set ups.

For observing the sediment transport pathways, a lot of fluorescent sand (in the order of 100-500 kg) is needed to have a chance to find small amounts of tracer sand back. When the wind has a large alongshore component, it might be that sediment injected in the intertidal zone travels several kilometers before it ends up close to the dunes. For such a large distance it is challenging to find any sand back, especially when only a small amount of sand is placed. To place enough sand on the beach (about 100-500 kg), a lot of effort and preparations would be required such as transporting the sand from the beach to the lab and back and painting the sand manually.

On the other hand, for observing the small scale dynamics of the injection site, a much smaller amount of sand (test site of ca. 30 x 30 cm) seems to be suitable. GoPro cameras from the side and the top relatively close to the injection site can be used to observe the dynamics. In order to have a high resolution of pixels per sand grain, a distance of max. 30 cm or less from the ground is preferred because then one pixel has approx. the size of 0.2 mm which is in the order of the mean grain size. For this set up, the sand does not even have to be fluorescent because the sediment dynamics of the test site can be tracked by the GoPro cameras during daylight.

The fluorescent characteristic is only of interest when looking into transport pathways because that would make it easier to find the tracer sand back into samples away from the injection site.

The set up for studying the dynamics of the injection site seems more feasible for this project because much less sand is required. This makes it easier to repeat and adjust the experiment. Therefore, the aim of test 02 is to test the applicability and feasibility of such an "injection site dynamics set up" by

- making videos with one GoPro camera from the top and one GoPro camera from the side at fixed positions,
- and implementing colored sand in an area of about 30 cm x 30 cm with a height of about 2 cm in the intertidal zone.

To take videos with the GoPro cameras from fixed positions, two frames are built to mount a GoPro cameras from the top and side of the test site. A black screen, parallel to the wind direction, is attached to the frame of the top camera in order to have a contrast in the background of the side view videos (figure A.2).



Figure A.2: Set up of test 02. One GoPro camera is attached to a vertical wood pole from the top, while the other one is mounted to a wood plate buried in the sand. A black screen is attached to the frame of the top view GoPro camera to provide a contrast in the side view video. During placing of the sand in an area of 30 cm x 30 cm with a height of about 2 cm, a removable wind protection screen is used to stop the tracer sand from being blown away. After placing the sand, this screen is removed. The tracer sand is transported to the beach in a bucket. Another bucket is used to collect sea water and create a moisture content of the tracer sand.

Placing the tracer sand in the intertidal zone is done in the same way as for test 01. The moisture content is created slightly differently. Sea water is slowly poured over the entire 30 cm x 30 cm injection site by using a shovel and is then mixed up with the colored sand by hand. The aim of this is to create a moisture content that mimics the one of the surrounding sand, that is not too wet and not too dry.

However, it is most likely that the tracer sand was wetter than the native sand because it did not erode much. Instead, it got covered with sand from the upwind direction. After one hour, there was still a thick red sand layer (right image, figure A.3). Therefore, dry red sand was placed on top of the moist red sand. The dry red sand got eroded and could be followed visually in downwind direction (left image, figure A.3). The red sand also interacted with the sand from the upwind direction and formed ripples (middle image, figure A.3).



Figure A.3: Observations during test 02. Right: Dry red tracer sand travels in wind direction. Middle: Dry red tracer sand interacts with sand from upwind direction and forms ripples. The ripples itself are moving in wind direction. Right: Moist red tracer sand did not erode much. After one hour most of it is still at the injection site.

A.3.1 Conclusions test 02

The camera set up worked well. The videos from the top view camera are very useful and many observations can be made. The videos from the side view camera show qualitatively up to which height sediment is in suspension. However, it is impossible to observe individual grains moving or to see how colored particles interact with non colored particles. For this, a different set up (e.g something similar to a PTV or PIV set up with a laser or LED light sheet) would be required.

Creating a moisture content of the tracer that mimics the surrounding sand is difficult. Is the sand too moist, almost no transport can be observed. For dry sand, a lot of transport and interaction with upwind sand can be observed. However, this might not mimic the behaviour of the surrounding sand because the surrounding sand is moist.

A.4 Test 03

After test 02 and while thinking about how to continue with this project, it turned out that the experimental set up is suitable to gain more insight into aeolian supply limiting factors. One of these factors is the moisture content. During test 01 and test 02, a clear difference between wet and dry tracer sand could be observed. However, it also turned out that it is very difficult to create the right moisture content for a certain area of the beach. This is important in order to make proper transport predictions for the different areas of the beach. Therefore, it is decided to first focus on other supply limiting factors, such as armoring effects and sorting processes, which might be possible to observe with this set up.

de Vries et al. (2014a) and Hoonhout and de Vries (2017) concluded from gradients in aeolian sediment transport observed during different field measurements in the Netherlands that the intertidal beach and not the dry beach functioned as primary source of aeolian sediment. The reason for this could be that a beach armor layer/the presence of lag deposits due to sediment sorting in the dry beach area outweighs the influence of high soil moisture contents in the intertidal beach area. In the intertidal beach area sediment is well-mixed due to marine processes, so that it can function as source for aeolian sediment transport.

A feasible goal with the set up described for test 02 could be to study armoring and sediment sorting processes in more detail and to gain more insight into the dynamics of the dry beach surface layer. The idea is to use different grain size fractions painted in different colors. The different fractions can be placed on the beach in different compositions, e.g. mixed, layered or striped. The GoPro cameras track what is happening with the different colored grains over time. Later on, the videos can be analyzed by counting the amount of pixels of a certain color over time.

To test the feasibility of this idea, test 03 is performed with the goal to test

- a slightly different set up than during test 02 with both GoPro cameras from the top, closer to the ground in order to have a higher resolution of pixels per sand grain,
- the implementation of dry tracer sand in the dry beach area,
- and how different colored grains can be observed in the videos.

For observing sediment sorting processes, the video from the top view might be more useful than the side view video. In order to have a higher resolution of pixels per sand grain, in this new set up both GoPro cameras are filming from the top view but closer to the ground. Using both cameras from the top enables to film an area of almost the same size as during test 02 but with a higher resolution. Both cameras are about 15 cm over the ground and are filming an area of about 30 cm x 17 cm (figure A.4). For a video resolution of 2.7K, this means that one pixel is in the order of 0.1 mm, which is about half the size of the mean grain diameter. Having a higher resolution might be useful for the post-processing of the videos.

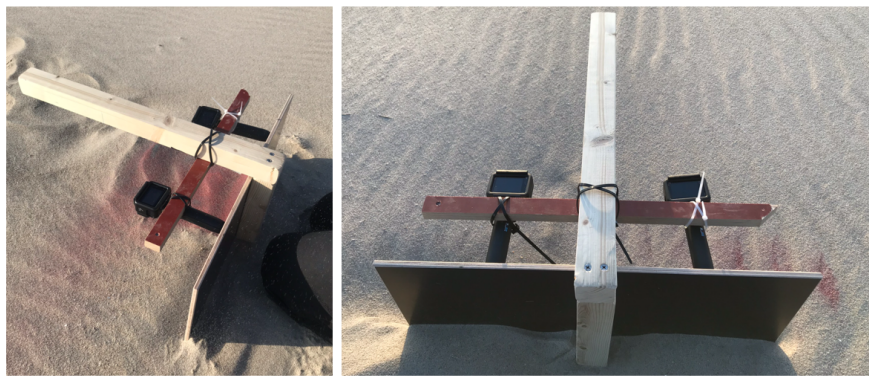


Figure A.4: Set up for test 03. Both GoPro cameras are taking videos from the top view. The cameras are closer to the ground than during test 02. The right GoPro camera in the right image takes videos from the injection site itself, while the left camera is taking videos from a site just downwind from the injection site. All grains that are leaving the right GoPro video are expected to enter the left GoPro video.

For implementing the colored sand in the field, the same method as for test 01 and test 02 is used. As the tracer sand is placed in the dry beach area, no moisture content is created.

The tracer sand used for test 03 is about 80 % red and 20 % blue. The red and blue sand is not mixed properly, so that after placing some blue patterns are visible in the mostly red sand. While doing the experiment it can be observed how some of the patterns are migrating in wind direction.



Figure A.5: Examples of blue patterns in red sand. Left: Colored sand placed at injection site just at the start of the experiment. Right: Screenshot out of video from right GoPro camera after tracer sand started moving.

In the beginning, it seems like the sand from upwind is covering the test site and the colored sand stays in place. However, after one hour, almost no tracer sand is found back at the injection site. This means that the colored

sand must have moved under the coverage of the upwind sand. This suggests that the active layer thickness is much larger than expected.

A.4.1 *Conclusions test 03*

The new camera set up worked well. The cameras were still far enough away from the injection site so that the videos are not blurred.

Implementing the tracer sand in the dry beach area makes it easier because no moisture content has to be created. The native sediment that got removed before placing the tracer sand seemed to have similar characteristics and to behave similar compared to the surrounding sand.

Different colored areas of sand can be visually distinguished in the video. This might be because the areas of different colored sand were relatively big because the red and blue sand fractions were not mixed properly. It is not clear yet whether individual grains of different color next to each other can be distinguished properly in the videos.

A.5 New research objective

After the first three tests, the research objective has changed quite a lot. Instead of using fluorescent sand and studying sediment transport pathways, the focus will solely be on the dynamics of the tracer injection site itself and how this is influenced by supply limiting factors such as armoring and sediment sorting processes. This study is presented in the main part of this report.

Tracer signature

B.1 Literature review

In order to label/create a 'signature' for the sand, the sand will be colored. From previous studies, different colouring procedures are known. Sutherland et al. (2000) for instance used black and white Tremclad rust spray paints to colour natural sediment. They used a rolling pin to eliminate any aggregates that may have occurred during the painting process.

According to Black et al. (2007), Teleki (1962) used fluorescent substance (both organic and non-organic) in a colloidal state to sand particles along with a binding material (e.g. agar or a resin), creating a tracer that caused no harm for the environment. Ingle (1966) used fluorescent dyes such as rhodamine (red) or anthracene (yellow-green) to coat natural sand particles (Black et al., 2007).

More recent studies, such as the one by Silva et al. (2007) for instance, give a very detailed description of the dyeing process. They used orange and blue fluorescent ink from Atomlac Industries (60% mass diluted with cellulosic solvent) and concentrated solid blue fluorescent ink from Risk Reactor combined with 10,000 parts of diluted varnish (70% varnish, 30% cellulosic solvent, portions by weight). The ratio ink/sand was 0.04 for Atomlac and 0.05 Risk Reactor inks. After they collected the sand from the beach, they washed it to remove salt, dried it in an open-air scatter over a plastic canvas and then painted it in concrete mixer in continuous motion. With this technique they produced 100 kg orange tracer (which they placed in a square of 4 m² on the beach with an average depth of 5 cm), plus additional 175 kg blue tracer (Silva et al., 2007).

According to Black et al. (2007), coating/dyeing sand particles for beach face dynamics studies is not problematic, with many studies undertaking the coating process using a cement mixer actually at the field site.

B.2 Procedure to create a tracer signature for this project

B.2.1 *Finding the right paint*

For this project it is important to find paint that is environmentally friendly and does not harm flora and fauna. The aim of this study is to develop a fieldwork method that is repeatable in the future at different beaches and therefore it is important that the paint has no negative impact.

To do so, different paint shops are approached and suitable paints are researched online. As a result, non-toxic fluorescent paint is found from Glowtec in the UK. Non-toxic, non-fluorescent paint is easier to get and available at common hardware stores. For this project, non-toxic red outside facade paint from Pufas and non-toxic Kids and School paint from Tempera in different colors are used.

Sutherland et al. (2000) used spray paint to color sand. To test the applicability of this method, fluorescent spray paint is used. Unfortunately, no non-toxic spray paint could be found, hence, neon spray paint from Dupli-Color is used for the tests.

B.2.2 *Coloring the sand*

Inspired from the literature review on different sand coloring procedures, different paints and painting methods are tested to color the sand for this project.

Fluorescent spray paint

The first test aims to test the applicability of fluorescent spray paint as a pre-painting method before using the colored sand on the beach. For this, a thin layer of sand is placed on a plastic bag (left image figure B.1), which is then colored by spraying fluorescent paint on it. While spraying, the sand grains start moving, clumps are forming and a few patches of sand are still without any paint (right image figure B.1).



Figure B.1: Coloring of sand with fluorescent spray paint before and after spraying.

To destroy the clumps and to distribute the paint better over all sand grains, plastic gloves are used. Unfortunately, the spray paint dries very quickly, so it is not possible to remove all clumps or to distribute the paint over all grains.

The second test, tests the applicability of fluorescent spray paint as *in situ* method at the beach. The paint is sprayed directly on the wet sand in the intertidal zone (figure B.2). The advantage of this method is that less clumps are forming because the moisture content of the sand in the intertidal zone stops individual grains from moving together. But it is still quite difficult to paint all grains even when a lot of paint is used. Besides that, the sand grains are sticking together after painting, which changes the erodibility characteristics of the colored sand compared to the native sand.



Figure B.2: With fluorescent spray paint colored sand in the intertidal zone at the beach.

In conclusion, the use of spray paint is neither suitable for pre-painting the sand nor to use it as an *in situ* method.

Fluorescent and non-fluorescent paint

The next attempt to color sand is to use a bucket of sand, a wood stick and non-toxic fluorescent paint from Glowtec (figure B.3). First, the sand is added to the bucket, then the paint is added, and after that, the wood stick is used to mix the two.



Figure B.3: Attempt to color sand in a bucket (right) with non-toxic fluorescent paint from Glowtec (left).

Immediately after adding the paint, clumps start forming, which are hard to remove with the wood stick. Additionally, it seems not possible to get a uniform sand-paint mixture with this method, especially not when relatively much sand (half a bucket) is used. This makes this method unsuitable to color large amounts of sand.

The next tested method is to use hands in plastic gloves and to manually mix the sand with the paint.



Figure B.4: Four steps to color sand manually by using hands in plastic gloves to mix the sand with the paint.

In the first step, sand is distributed evenly over a plastic bag. Then, paint is poured over the sand (step 2) and mixed up with the sand by using hands in plastic gloves (step 3). For this step it is important to properly rub the sand between the hands for a few times to remove all clumps. After that, the sand is distributed evenly over to plastic bag again in order to dry.

This method turned out to be successful for all fluorescent and non-fluorescent paints that were tested. But it is important to find the right paint/sand ratio for every paint. In case too much paint is used, the grains start sticking together while drying. The more paint is used, the firmer the paint-sand mixture gets and the harder it is to break it down into individual grains afterwards (figure B.5). The fluorescent paint from Glowtec was slightly more sticky than all other non-fluorescent paints that were tested.



Figure B.5: Examples of too much paint. Sand and paint are sticking together after drying and it is almost impossible to break it down into individual grains. Left: Mixture of sand and green fluorescent paint from Glowtec. Right: Mixture of sand and pink fluorescent paint from Glowtec.

On the other hand, in case too less paint is used, the color intensity decreases and it gets harder to distinguish the colored sand from the native sand (figure B.6).



Figure B.6: Examples of paint-sand mixtures with different paint/sand ratios. Top: Colored sand after drying. The paint/sand ratio on the left is smaller than on the right. Bottom left: Sand grains from top left image under microscope. Bottom right: Sand grains from the top right image under the microscope. The color intensity of the right sand is higher compared to the sand on the left.

In conclusion, the second method described (figure B.4) is suitable for pre-coloring the sand before implementing in the field. This means that sand is taken from the beach, brought to the lab, colored and dried in the lab and then brought back to the beach for doing the experiments.

Grain size distribution before and after painting

For a tracer study it is fundamental that the tracer mimics the behaviour of the target sediments adequately and this must remain for the duration of the experiment (Black et al., 2007). The most important characteristic of the tracer sand compared to the native sand is the grain size.

To compare the grain size distribution before and after painting, a sieve analysis is done. A sample for 826.6 g is sieved and weighted per fraction. From this, a particle size distribution (PSD) is derived (blue line, figure B.7). After that, the same sample is painted and dried. The sample weight slightly increased to 831.8 g. The sample is sieved and weighted per fraction again and a second PSD is derived (pink line, figure B.7).

Table B.1: Different fractions with indication of grain size range and color that are used for coloring the sand.

Fraction	Grain size range [mm]	Color
1	0.3 - 0.6	Red
2	0.25 - 0.3	Blue
3	0.18 - 0.25	green
4	< 0.18	purple

To obtain the different fractions from the native sand, all sand, that is collected from the beach, must be sieved. For this, a sieve tower with shaking function is used. After adding a shovel of sand (ca. 800 g) to the tower, it is shaking for 15 minutes. Then the sand is added to different buckets.

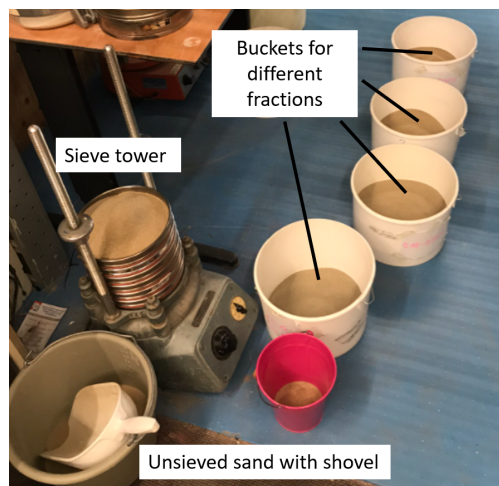


Figure B.9: Sieving sand from the beach in the lab by using a sieve tower. Different fractions are put in different buckets afterwards.

After sieving, the sand is colored with non-toxic paint from Tempera in different colors according to table B.1 with the method described in figure B.4. Once the sand is dry after coloring, it is sieved again to remove clumps and to break up grains that are sticking together. Additionally, all colored grains that are too big or too small for one of the fractions after sieving get removed. This procedure results in grains that can be clearly distinguished in size under the microscope and in color (figure B.10).

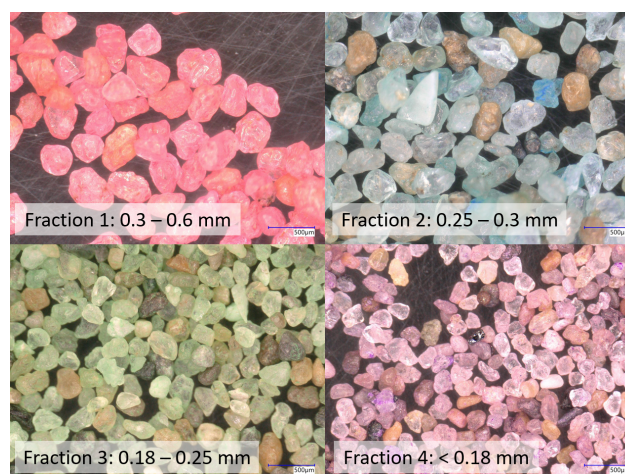


Figure B.10: Colored sand under the microscope per fraction. All images are at the same scale, which means that the size difference visible here is the actual size difference.



User's manual wind measurement device

This user manual aims to summarize the most important steps how to work with the existing wind measurement equipment from TU Delft without spending a lot of time reading the HOBO Energy Logger User's Guide, the HOBOWare User's Guide, and the Gill WindSonic User Manual. However, in case more information is required, this are the links to the above mentioned manuals:

- HOBO Energy Logger User's Guide:
https://www.onsetcomp.com/files/manual_pdfs/9857-I%20MAN-H22-web.pdf
- HOBOWare User's Guide:
https://www.onsetcomp.com/files/manual_pdfs/12730-AD%20HOBOWare%20User%27s%20Guide.pdf
- Gill WindSonic User Manual:
<http://gillinstruments.com/data/manuals/1405-PS-0019%20WindSonic%20GPA%20manual%20issue%2028.pdf>

C.1 Step 1: Checking equipment

Before you start, check if all required equipment is available.

The measurement equipment contains of:

- Gill 2D WindSonic ultrasonic wind speed and direction sensor (P/N:1405-PK-040) (Figure C.1 a))
- HOBO Energy data logger (P/N: H22-001) incl. FlexSmart Analog device and internal batteries (Figure C.2)
- External battery incl. connection cable to data logger
- Orange suitcase to store data logger and external battery (Figure C.1 a))
- 1.80 m metal pole (Figure C.1 a); stored in jetski corner of Waterlab)
- Connection cable consisting of 9 wires to connect wind sensor and data logger (attached to metal pole) (Figures C.1 a) and C.2)
- Small screw driver to connect cable to FlexModule Analog device

To start the wind measurement device and read out the data, the following is needed:

- Laptop
- Free HOBOWare (can be downloaded via: <https://www.onsetcomp.com/hoboware-free-download/>)
- Connection cable for laptop and data logger incl. RS232 to USB converter
- Correct driver for RS232 to USB converter on laptop

To install the measurement equipment in the field, the following is needed:

- Rubber mallet to hammer the metal pole into the ground
- Wood piece to put between mallet and metal pole during hammering
- Screws to attach the wind sensor to the metal pole
- Extra batteries

- Compass to orientate the wind sensor in northern direction
- Spirit level to align the metal pole vertically

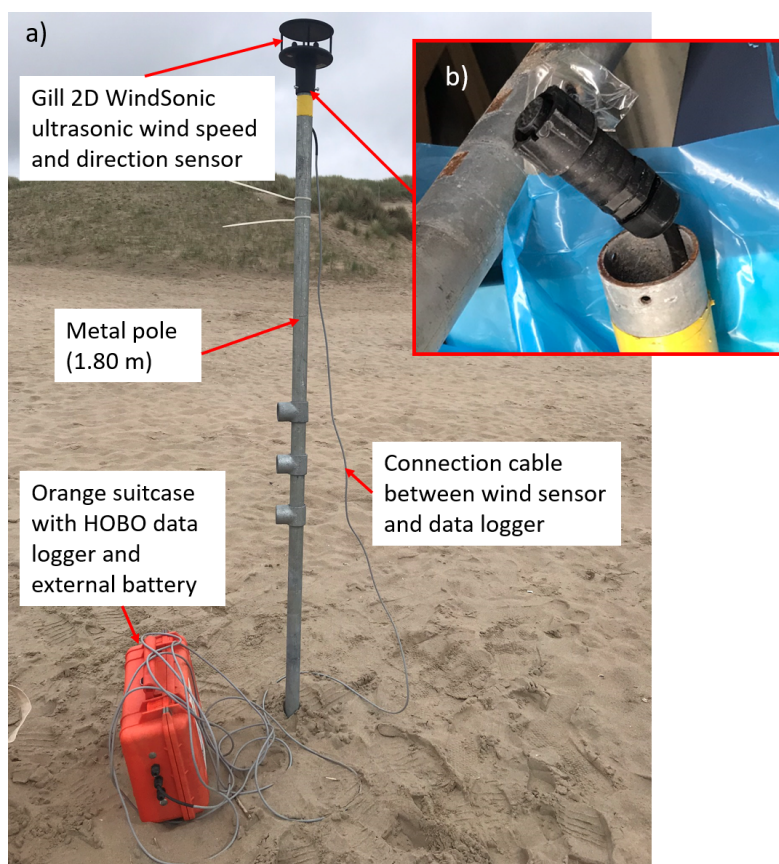


Figure C.1: Overview of wind measurement device. a) Shows the device build up in the field. b) Shows the connector piece of the cable to attach it to the wind sensor.

C.2 Step 2: Set up wind measurement device

Once all measurement equipment is complete, the data logger with one FlexSmart Analog device, internal batteries and one big external battery can be placed in the orange suitcase. The data logger can be connected to the wind sensor by using the cable attached to the metal pole. The cable consists of nine wires which are attached to a black connector at the upper end of the metal pole (Figure C.1 b)). This connector fits on the bottom part of the wind sensor. At the lower end of the metal pole, the nine different colored wires are visible. Detach the FlexSmart Analog device from the data logger (to make sure no electricity flows through the device) and connect six of the wires through a hole in the orange suitcase to the FlexSmart Analog device with the colors according to Figure C.2 (Shld: black, S1+: grey, S1-: brown, Exc+: red, Exc-: light pin, S2+: white, S2-: none). The remaining wires stay unconnected. Reattach the FlexSmart Analog device to the data logger. Connect the data logger to the external battery before using it and detach it every time after using it. Now the device is set up for use.

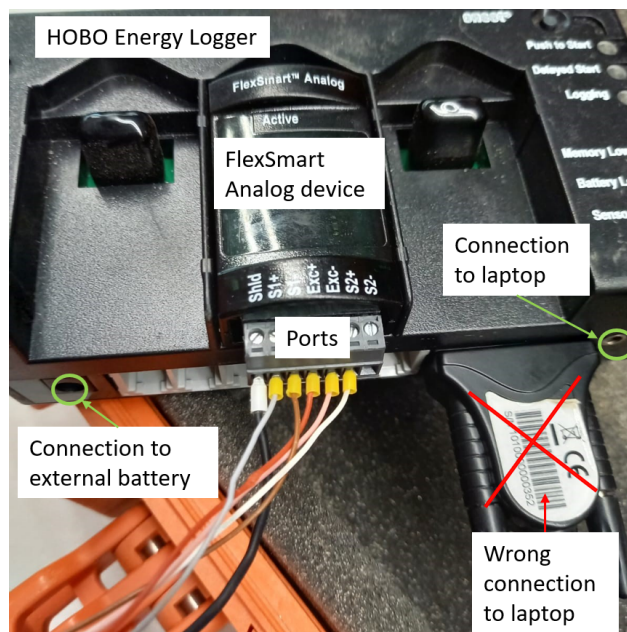


Figure C.2: Overview of HOBO Energy Logger with FlexSmart Analog device and connections

C.3 Step 3: Connecting data logger with laptop to start and read device

Before connecting the data logger with a laptop, install the free version of HOBOWare via the link above on that laptop. Also make sure to have all drivers on the laptop which are needed for the RS232 to USB converter. Connect the grey connection cable with the converter and then the converter with the laptop via an USB port. The other end of the grey cable has to be connected to the data logger via the small, round port and not via the bigger port next to it (Figure C.2).

Now HOBOWare can be opened. the first step is to click the 'Select Device' icon on the toolbar to ensure that the device is listed in the Select Device window. Click the button next to the device in the window, then click 'OK'. The software is very user-friendly and mostly self-explanatory. For more information the user is referred to the HOBOWare User's Guide. One important thing that must be noticed is that sensor sends signals to the data logger in the unit 'mA' if no scaling relationship is defined. Before logging is started, it can be helpful to define the following scaling relationship for wind speed: $4mA = 0m/s$ and $20mA = 32.4m/s$, and for wind direction: $4mA = 0^\circ$ and $20mA = 360^\circ$. Then the data will be returned in m/s and $^\circ$ instead of mA . However, this relationship might be different for every individual sensor and it is therefore important to calibrate it (see step 4). In case the scaling relationship is not defined before logging, it can still be defined afterwards when plotting the data. However, it can make the plotting process more time consuming and therefore it is recommended to do it beforehand.

C.4 Step 4: Preliminary tests and calibration

Before taking the wind measurement device to the field, make sure the device runs as supposed to by testing different angles where the wind is coming from and different wind speeds. This can be done by using the wind machine from the wind tunnel for instance which can be set on different wind speeds. Different wind directions can be tested by changing the orientation of the sensor (North arrow on sensor can be pointed into different directions). When evaluating the recorded data later on and relating it to the tested wind speeds and angles, the wind measurement device can be calibrated.

C.5 Step 5: Using the wind measurement device in the field

Pack all equipment needed for setting up the measurement device in the field (list step 1). Be aware of the sandy conditions in the field when using it at the beach on a windy day. To start the data logger, it has to be taken out of the orange suitcase. Therefore, it might be wise to start the data logger with a laptop from home, or when possible at a sheltered spot on the beach to prevent sand from getting into the logger when connecting it with a laptop. For starting the device two options seem suitable: 1.) Starting the logger while it is connected to the laptop, 2.) Choosing the option 'Push Start' while the logger is connected to the laptop, so that the data logger will start logging after the black button on the logger is pushed. A green light on the logger blinks when logging is started successfully.

After the logger is safely stored in the orange suitcase again, bring all equipment to the desired measurement location. Hammer the metal pole into the ground by using the wood piece in between the pole and the rubber mallet. Use the spirit level to align the metal pole vertically. Connect the wind sensor to the connector piece of the cable and screw it to the metal pole. Use the compass to orientate the small arrow on the wind sensor in northern direction by rotating the metal pole. Now the measurement device is ready to perform measurements. In case it is planned to do measurements for a long time, check the external battery of the device. It is possible to exchange the external battery without gaps in the measurements series when the data logger is equipped with additional internal batteries.

C.6 Step 6: Reading out the data logger

When all measurements are done, remove the wind measurement device from the field. To stop the data logger, connect it with a laptop and save the recorded data. It is possible to export the data as an Excel file via HOBOWare or to do plots with HOBOWare directly.

C.7 Step 7: Cleaning and storing of equipment

After using the equipment and performing measurements, clean all pieces from sand and salt water for the next user. Especially metal connections are sensitive to corrosion. Bring all parts back to where they came from.

Image analysis by using a pixel color recognition algorithm

D.1 Microscope images

In order to analyse the stitched images taken by a digital microscope from all 59 samples, a pixel color recognition algorithm (see below) counting the red, green, blue and purple pixels in every image was used. The stitched images have a high resolution, therefore they need to be broken down into smaller blocks of 10,000 x 10,000 pixels each in order to process them.

The color range for the red, green, blue and purple pixels was defined by using the color picker tool of the free software GIMP. For several different pixels of different red, green, blue and purple grains the HSV value was determined from which then a range for hue, saturation and value was derived. The most distinct parameter is the hue, which is defined in the pixel color recognition algorithm as illustrated in figure D.1.

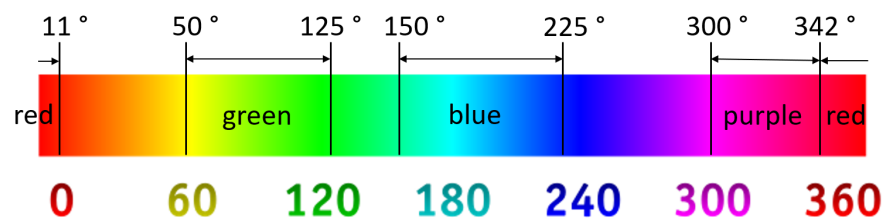


Figure D.1: Illustration of the hue range for red, green, blue and purple grains used for the analysis of the microscope images.

In figure D.2 an example is presented that shows which pixels are captured by the pixel color recognition algorithm. For all captured pixels, the saturation is increased, so that they are more visible in the figure. Most pixels of the colored grains are captured but not all. Additionally, some pixels of non-colored grains fall in the defined HSV range of a certain color and count erroneously as pixels of the colored grains. To test the accuracy of the pixel color recognition algorithm, three stitched images of samples with only non-colored grains were used. For this the code counted about 0.1 % colored pixels relative to all pixels in the image. Therefore, only images where the amount of counted, colored pixels are larger than 1 % were taken into account for the analysis. Otherwise the influence of the erroneously counted pixels of non-colored grains becomes too much and distorts the results.

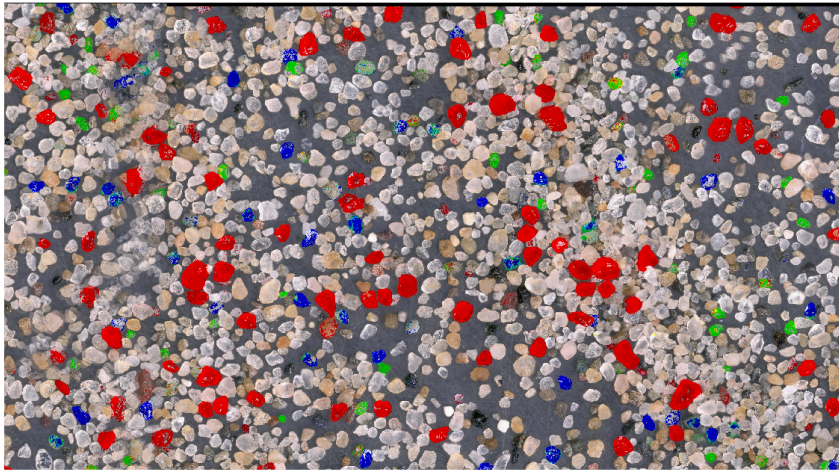


Figure D.2: Extract from the stitched microscope image of a sample with pixels captured by the pixel color recognition algorithm are highlighted due to an increased saturation.

```

clc;      % Clear the command window.
close all; % Close all figures (except those of imtool.)
clear;

rgbImage = imread('14_00.jpg');

[rows columns numberOfColorBands] = size(rgbImage) % Get the dimensions of the image
=====
%Divide the image into blocks that will be analysed
% The first way to divide an image up into blocks is by using mat2cell().
blockSizeR = 10000; % Rows in block.
blockSizeC = 10000; % Columns in block.
% Most will be blockSizeR but there may be a remainder amount of less than that.
wholeBlockRows = floor(rows / blockSizeR);
blockVectorR = [blockSizeR * ones(1, wholeBlockRows), rem(rows, blockSizeR)];

wholeBlockCols = floor(columns / blockSizeC);
blockVectorC = [blockSizeC * ones(1, wholeBlockCols), rem(columns, blockSizeC)];
% Create the cell array, ca.
% Each cell (except for the remainder cells at the end of the image)
% in the array contains a blockSizeR by blockSizeC by 3 color array.
% This line is where the image is actually divided up into blocks.
if numberOfColorBands > 1
    % It's a color image.
    ca = mat2cell(rgbImage, blockVectorR, blockVectorC, numberOfColorBands);
else
    ca = mat2cell(rgbImage, blockVectorR, blockVectorC);
end
% Now display all the blocks.
plotIndex = 1;
numPlotsR = size(ca, 1);
numPlotsC = size(ca, 2);

%Define empty a matrix for every color that will get filled during the for
%loop
blue=zeros(numPlotsR,numPlotsC);
green=zeros(numPlotsR,numPlotsC);
purple=zeros(numPlotsR,numPlotsC);
red=zeros(numPlotsR,numPlotsC);
colored=zeros(numPlotsR,numPlotsC);

=====
%Analyse every block

for r = 1 : numPlotsR
    for c = 1 : numPlotsC

        rgbBlock = ca{r,c};

        %Convert RGB color space into HSV color space
        hsv = rgb2hsv(rgbBlock);
        hueImage = hsv(:, :, 1);
        saturationImage = hsv(:, :, 2);
        valueImage = hsv(:, :, 3);
    end
end

```

```

%Define color range for blue, red, green and purple

bluePixels = hueImage > 0.415 & hueImage < 0.626 & saturationImage > 0.02 & saturationImage < 0.2 & valueImage > 0.5 & valueImage < 0.9; %& valueImage < 0.8;
redPixels = hueImage > 0.95 & saturationImage > 0.25 & saturationImage < 0.65 & valueImage > 0.55 | hueImage < 0.03 & saturationImage > 0.25 & saturationImage < 0.65 & valueImage > 0.55;
greenPixels = hueImage > 0.138 & hueImage < 0.35 & saturationImage > 0.1 & saturationImage < 0.25 & valueImage > 0.5 & valueImage < 0.9 | hueImage > 0.125 & hueImage < 0.353 & saturationImage > 0.03 & saturationImage < 0.25 & valueImage > 0.7; %& valueImage < 0.8;
purplePixels = hueImage > 0.84 & hueImage < 0.95 & saturationImage > 0.1 & saturationImage < 0.3 & valueImage > 0.4 & valueImage < 0.70; %& valueImage < 0.8;
coloredPixels = hueImage > 0.415 & hueImage < 0.626 & saturationImage > 0.02 & saturationImage < 0.2 & valueImage > 0.5 & valueImage < 0.9 | hueImage > 0.95 & saturationImage > 0.25 & saturationImage < 0.65 & valueImage > 0.55 | hueImage < 0.03 & saturationImage > 0.25 & saturationImage < 0.65 & valueImage > 0.55 | hueImage > 0.138 & hueImage < 0.35 & saturationImage > 0.1 & saturationImage < 0.25 & valueImage > 0.5 & valueImage < 0.9 | hueImage > 0.125 & hueImage < 0.353 & saturationImage > 0.03 & saturationImage < 0.25 & valueImage > 0.7 | hueImage > 0.84 & hueImage < 0.95 & saturationImage > 0.1 & saturationImage < 0.3 & valueImage > 0.4 & valueImage < 0.70;

%Calculate total amount of pixels of every color
bP = sum(sum(bluePixels));
rP = sum(sum(redPixels));
gP = sum(sum(greenPixels));
pP = sum(sum(purplePixels));
cP = sum(sum(coloredPixels));

%For every block: Write total amount of every color in pre-defined matrix
red(r,c) = rP;
blue(r,c) = bP;
green(r,c) = gP;
purple(r,c) = pP;
colored(r,c) = cP;

%Plot one figure for every block containing of the block image, and
%five black and white images showing the pixels of a certain color in
%white and the remaining pixels in black
figure;
subplot(2, 3, 1);
imshow(rgbBlock);
subplot(2, 3, 2);
imshow(bluePixels);
title('blue Pixels');
subplot(2, 3, 3);
imshow(redPixels);
title('red Pixels');
subplot(2, 3, 6);
imshow(coloredPixels);
title('colored Pixels');
subplot(2, 3, 4);
imshow(greenPixels);
title('green Pixels');
subplot(2, 3, 5);
imshow(purplePixels);
title('purple Pixels');

```

```

end
end

%=====
%Calculation of total amount of pixels of a certain color for whole image
%(summation of all blocks)
redtot=sum(sum(red))
greentot=sum(sum(green))
bluetot=sum(sum(blue))
purpletot=sum(sum(purple))
colortot=sum(sum(colored))

%Normalization of amount of pixels by dividing the amount of pixels of a
%certain color by the total amount of colored pixels
percentRed=redtot/colortot
percentGreen=greentot/colortot
percentBlue=bluetot/colortot
percentPurple=purpletot/colortot

%Calculation of total amount of colored pixels relative to all pixels of the
%image
%(When this is smaller than 0.01, the importance of the non-colored sand grains
%that fall in the range of the previously defined HSV ranges becomes too
%large)
all=rows*columns;
percentColored=colortot/all

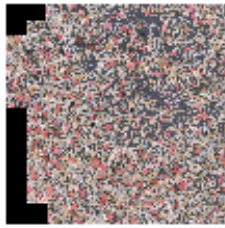
```

```

rows =
    19575
columns =
    19779
numberOfColorBands =
    3
redtot =
    23726436
greentot =
    4341212
bluetot =
    6232028
purpletot =
    717867
colortot =
    35017543
percentRed =
    0.677558559719624
percentGreen =
    0.123972490017361
percentBlue =
    0.177968739839914
percentPurple =
    0.0205002104231014
percentColored =

```

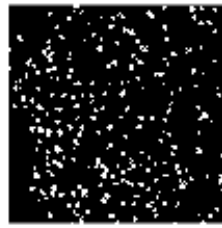
0.0904439600368232



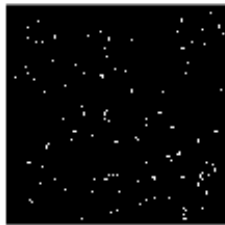
blue Pixels



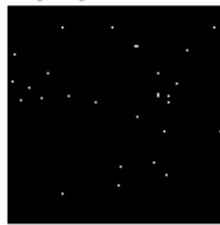
red Pixels



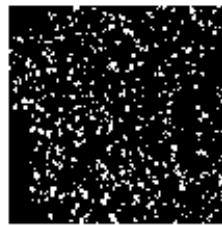
green Pixels



purple Pixels

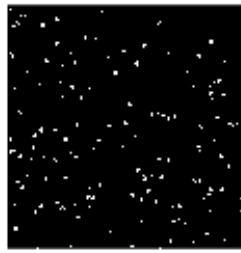


colored Pixels

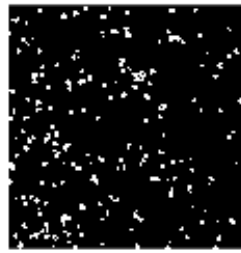




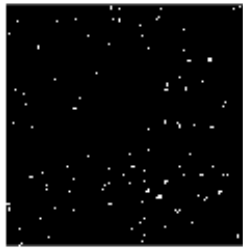
blue Pixels



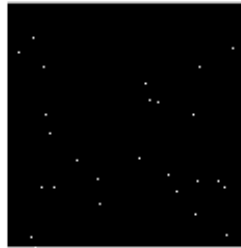
red Pixels



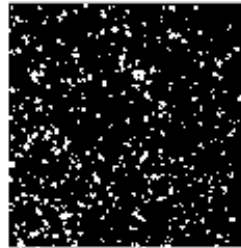
green Pixels



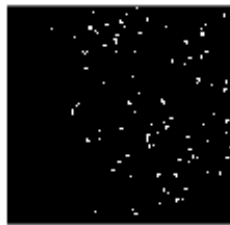
purple Pixels



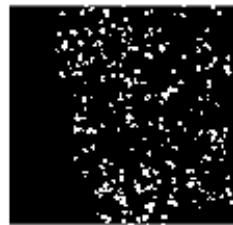
colored Pixels



blue Pixels



red Pixels



green Pixels



purple Pixels



colored Pixels





blue Pixels



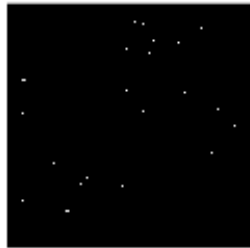
red Pixels



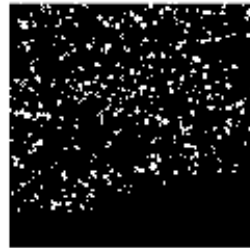
green Pixels



purple Pixels



colored Pixels



D.2 GoPro images

The analysis of the top view GoPro images is similar to the one of the microscope images. A pixel color recognition algorithm (see below) counting the red, green, blue and purple pixels in every image was used. The color range for the red, green, blue and purple pixels was defined by using the color picker tool of the free software GIMP and slightly differs from the one of the microscope images (figure D.3).

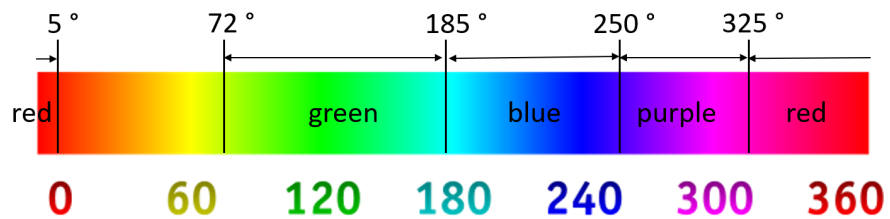


Figure D.3: Illustration of the hue range for red, green, blue and purple grains used for the analysis of the GoPro images.

To obtain the evolution of different colored pixels over time, a loop over all images is done, which is then plotted in different graphs.

```

clc;      % Clear the command window.
close all; % Close all figures (except those of imtool.)
clear;
myFolder = 'P:\MSc Project\GoPro\05_23\GoProII\M_R03'; % Specify the folder where the files
live.

% Get a list of all files in the folder with the desired file name pattern.
filePattern = fullfile(myFolder, '*.jpg'); % Change to whatever pattern you need.
theFiles = dir(filePattern);

%Create empty color vectors
m=length(theFiles);%Number of postprocessing images
blue=zeros(1,m);
green=zeros(1,m);
purple=zeros(1,m);
purplec=zeros(1,m);
greenc=zeros(1,m);
cc=zeros(1,m);
bluec=zeros(1,m);
redc=zeros(1,m);
red=zeros(1,m);
alle=zeros(1,m);
for k = 1 : length(theFiles)
    baseFileName = theFiles(k).name;
    fullFileName = fullfile(theFiles(k).folder, baseFileName);

    rgbImage = imread(fullFileName);
    %[rows columns numberOfColorBands] = size(rgbImage);

    %Transfer RGB spectrum to HSV spectrum
    hsv = rgb2hsv(rgbImage);
    hueImage = hsv(:, :, 1);
    saturationImage = hsv(:, :, 2);
    valueImage = hsv(:, :, 3);

    %Define color range for blue, red, green and purple pixels

    bluePixels = hueImage > 0.52 & hueImage < 0.7 & saturationImage > 0.07&saturationImage
< 0.25 &valueImage > 0.4 &valueImage < 0.7;

    redPixels = hueImage > 0.85 &saturationImage > 0.12 & valueImage > 0.5| hueImage < 0.0
1&saturationImage > 0.14&valueImage>0.35;

    greenPixels = hueImage > 0.2 & hueImage < 0.52&saturationImage>0.06;

    purplePixels = hueImage > 0.7 & hueImage < 0.9&saturationImage>0.05&saturationImage<0.
2& valueImage > 0.4& valueImage < 0.6;

    %Calculate the amount of pixels of one color in one image relative to all pixels of tha
t image
    percentBlue = 100*(sum(sum(bluePixels))/(size(rgbImage,1)*size(rgbImage,2)));
    percentRed=100*(sum(sum(redPixels))/(size(rgbImage,1)*size(rgbImage,2)));
    percentGreen=100*(sum(sum(greenPixels))/(size(rgbImage,1)*size(rgbImage,2)));
    percentPurple=100*(sum(sum(purplePixels))/(size(rgbImage,1)*size(rgbImage,2)));

```

```

%Calculate the amount of all colored pixels
%colored=sum(sum(redPixels))+sum(sum(greenPixels))+sum(sum(bluePixels))+sum(sum(purple
Pixels))%When all colors are used
colored=sum(sum(redPixels))+sum(sum(greenPixels));%For only red and green
coloredc=100*(colored/(size(rgbImage,1)*size(rgbImage,2)));

%Percent of red and green pixels in the image
pRoc=100*(sum(sum(redPixels))/colored); %Percent of red pixels of all colored pixels
pGoc=100*(sum(sum(greenPixels))/colored);%Percent of green pixels of all colored pixel
s

%Fill empty vectors with the numbers of every image
cc(1,k)=coloredc;
green(1,k)=percentGreen;
greenc(1,k)=pGoc;
redc(1,k)=pRoc;
red(1,k)=percentRed;

end

%Timevector
deltat=1.0;%time difference between two images IN SECONDS
totduration=(m*deltat)-deltat;
ts = 0:deltat:totduration;

%Plots for color evolution of red and green pixels
subplot(2, 1, 1);
plot(ts,red,'r',ts,green,'g')
title('Amount of red and green sand over time'); xlabel('Time [seconds]');ylabel('Red and
green pixels/All pixels [%]')
grid on

figure;
subplot(2, 1, 1);
plot(ts,redc,'r',ts,greenc,'g');
title('Amount of different colored sand over time'); xlabel('Time [seconds]');ylabel('Pixe
ls of one color/All colored pixels [%]')
legend('red','green')
grid on

subplot(2, 1, 2);
plot(ts,cc,'color',[.5 .0 .5] );
title('Amount of colored sand over time'); xlabel('Time [seconds]');ylabel('Colored pixels
/All pixels [%]')
axis([0 inf 0 100])
grid on

% %Plots for color evolution of red, green, blue and purple pixels
% figure;
% subplot(5, 1, 1);
% plot(ts,cc,'color',[.7 .67 .63]);
% title('Amount of colored sand over time'); xlabel('Time [seconds]');ylabel('Colored pixe
ls/All pixels[%]')
% grid on
%
% subplot(5, 1, 2);

```

```

% plot(ts,blue,'b');
% title('Amount of blue sand over time'); xlabel('Time [seconds]');ylabel('Blue pixels/All
pixels [%]')
% grid on
%
% subplot(5, 1, 3);
% plot(ts,red,'r')
% title('Amount of red sand over time'); xlabel('Time [seconds]');ylabel('Red pixels/All p
ixels [%]')
% grid on
%
% subplot(5, 1, 4);
% plot(ts,green,'g')
% title('Amount of green sand over time'); xlabel('Time [seconds]');ylabel('Green pixels/A
ll pixels [%]')
% grid on
%
% subplot(5, 1, 5);
% plot(ts,purple,'m')
% title('Amount of purple sand over time'); xlabel('Time [seconds]');ylabel('Purple pixels
/All pixels [%]')
% grid on
%
% figure;
% plot(ts,alle);
% title('Amount of pixels captured by Matlab code'); xlabel('Time [seconds]');ylabel('Capt
ured pixels/All pixels [%]')
% grid on
%
% figure;
% plot(ts,blue,'b',ts,red,'r',ts,green,'g',ts,purple,'m');
% title('Amount of different colored sand over time'); xlabel('Time [seconds]');ylabel('Co
lored pixels/All pixels [%]')
% legend('blue','red','green','purple')
% grid on
%
% figure;
% subplot(2, 1, 1);
% plot(ts,bluec,'b',ts,redc,'r',ts,greenc,'g',ts,purplec,'m');
% title('Amount of different colored sand over time'); xlabel('Time [seconds]');ylabel('Pi
xels of one color/All colored pixels [%]')
% legend('blue','red','green','purple')
% grid on
%
% subplot(2, 1, 2);
% plot(ts,cc,'color',[.5 .0 .5] );
% title('Amount of colored sand over time'); xlabel('Time [seconds]');ylabel('Colored pixe
ls/All pixels [%]')
% axis([0 inf 0 100])
% grid on

```

